# MOUNTAIN-PLAINS CONSORTIUM

**MPC 24-541** | A.D. Sorensen and J. Jiang

# STATIC AND DYNAMIC EXPERIMENTAL EVALUATION OF PRECAST COLUMNS WITH GROUTED SPLICE SLEEVE CONNECTORS


MOUNTAIN-PLAINS CONSORTIUM REGION 8

A University Transportation Center sponsored by the U.S. Department of Transportation serving the Mountain-Plains Region. Consortium members:

Colorado State University
North Dakota State University
South Dakota State University
University of Colorado Denver
University of Denver
University of Utah
Utah State University
University of Wyoming

**Technical Report Documentation Page**

| 1. Report No. | 2. Government Accession No. | 3. Recipient's Catalog No. |
|---|---|---|
| MPC-623 | | |

| 4. Title and Subtitle | 5. Report Date |
|---|---|
| Static and Dynamic Experimental Evaluation of Precast Columns with Grouted Splice Sleeve Connectors | August 2024 |
| | 6. Performing Organization Code |

| 7. Author(s) | 8. Performing Organization Report No. |
|---|---|
| Andrew D. Sorensen<br>Jinghui Jiang | MPC 24-541 |

| 9. Performing Organization Name and Address | 10. Work Unit No. (TRAIS) |
|---|---|
| Utah State University<br>4110 Old Main Hill<br>Logan, UT, 84322-4110 | 11. Contract or Grant No. |

| 12. Sponsoring Agency Name and Address | 13. Type of Report and Period Covered |
|---|---|
| Mountain-Plains Consortium<br>North Dakota State University<br>PO Box 6050, Fargo, ND 58108 | Final Report |
| | 14. Sponsoring Agency Code |

15. Supplementary Notes

Supported by a grant from the US DOT, University Transportation Centers Program

16. Abstract

With the popularization of accelerated bridge construction (ABC), the utilization of splice sleeve connections has been researched to determine their performance using a variety of connection details and under several loading scenarios. However, fundamental research on the load distribution and load transfer mechanism within the sleeve region under the combination of compressive and shear loads are limited. Additionally, a few studies have conducted the dynamic analysis of the coupler (i.e. coupler, rebar and grout), but to date, no study can be found that assesses the connections in sequence with the encasing concrete to detail the load paths for the composite member, evaluates the dynamic behavior and failure modes of precast columns with connections at different locations columns under low-velocity impact loading, nor that determines non-visible damage within the post-impact sleeve. In this study, two groups of precast concrete specimens with grouted splice sleeve (GSS) connectors at different locations are tested. The two groups represent two typical connection details for bridge piers to footings: one with the sleeve in the top of the footing and one in with the coupler at the base of the column. This study is divided into two major parts: static and dynamic investigations.

The static part attempts to investigate the material load-bearing percentages and forces' transmission rules of grouted, splice sleeve connections encased in a normal strength Portland cement concrete mixture. The findings indicate that the structure with the top of footing connection presents a better anti-lateral load performance than those with pier base connection. Based on the measured data, the load distribution percentage of each component of the GSS system (i.e. rebar, coupler, grout, and concrete) is then determined and compared with theoretical predictions, and the comparisons reveal that rebars on both ends of the coupler carry 11% to 26% more load than theoretical predictions, which may lead to a potential risk of rebar fracture. Mechanics of load transfer on structure are explained as three main load paths, and force transfer principles in the GSS region are further detailed.

In dynamic testing, the impact responses and failure processes of specimens are contrasted between the two categories of connectors. Subsequently, pull-out tests are performed on post-impact GGS connectors to reveal the failure modes and bond strength reduction percentage of post-damage couplers. The findings indicate that structure with the top of footing connection exhibits a more ductile response and better impact resistance than those with pier base connection. Based on the final failure patterns, most specimens maintain the GSS connections' integrity and bond performance after impact loading, with major damage enacted as diagonal shear fractures occurring away from the GSS regions. Failure modes of post-impact couplers vary significantly with the connection type; GSS-F specimens show rebar tensile fractures near the coupler, while GSS-C specimens experience bond-slip failures at the narrow end. Moreover, GSS-F couplers exhibit minimal tensile capacity reduction (4%-5%), demonstrating perfect bond integrity after impact, in contrast to GSS-C couplers, which show substantial tensile strength reductions of 10% and 98%.

This study not only provides novel and in-depth insights into theoretical research on the mechanism of precast concrete construction utilizing a GSS system, but also contributes much-needed data of impact test of the precast columns and novel insights into residual bond strength analysis of the post-impact GSS connectors.

| 17. Key Word | 18. Distribution Statement |
|---|---|
| Grouted splice sleeve connectors; Precast pier | Public distribution |

| 19. Security Classif. (of this report) | 20. Security Classif. (of this page) | 21. No. of Pages | 22. Price |
|---|---|---|---|
| Unclassified | Unclassified | 66 | n/a |

# Static and Dynamic Experimental Evaluation of Precast Columns with Grouted Splice Sleeve Connectors

Andrew D. Sorensen
Jinghui Jiang

Utah State University
Logan, Utah

August 2024

## ACKNOWLEDGMENTS

The authors would like to acknowledge the Mountain-Plains Consortium (MPC)-University Transportation Center sponsored by the U.S. Department of Transportation for providing the research funding to support this study. Additionally, the authors would like to thank Splice Sleeve North America, Inc., for their contribution of the couplers and grout studied in this project. In addition, the authors would also like to acknowledge our research group members: Ashesh Pokhrel, Abdullah (Ony) Al Sarfin, and Zach Benson, who provided valuable assistance in experiments during this project.

## DISCLAIMER

The contents of this report reflect the views of the authors, who are responsible for the facts and the accuracy of the information presented. This document is disseminated under the sponsorship of the Department of Transportation, University Transportation Centers Program, in the interest of information exchange. The U.S. Government assumes no liability for the contents or use thereof.

# ABSTRACT

With the popularization of accelerated bridge construction (ABC), the utilization of splice sleeve connections has been researched to determine their performance using a variety of connection details and under several loading scenarios. However, fundamental research on the load distribution and load transfer mechanism within the sleeve region under the combination of compressive and shear loads are limited. Additionally, a few studies have conducted the dynamic analysis of the coupler (i.e., coupler, rebar, and grout). But to date, no study can be found that assesses the connections in sequence with the encasing concrete to detail the load paths for the composite member, evaluates the dynamic behavior and failure modes of precast columns with connections at different column locations under low-velocity impact loading, or determines non-visible damage within the post-impact sleeve. In this study, two groups of precast concrete specimens with grouted splice sleeve (GSS) connectors at different locations are tested. The two groups represent two typical connection details for bridge piers to footings: one with the sleeve in the top of the footing and one in with the coupler at the base of the column. This study is divided into two major parts: static and dynamic investigations.

The static part attempts to investigate the material load-bearing percentages and force transmission rules of grouted splice sleeve connections encased in a normal strength Portland cement concrete mixture. The findings indicate that the structure with the top-of-footing connection presents a better anti-lateral load performance than those with the pier base connection. Based on the measured data, the load distribution percentage of each GSS system component (i.e., rebar, coupler, grout, and concrete) is then determined and compared with theoretical predictions, and the comparisons reveal that rebars on both ends of the coupler carry 11% to 26% more load than theoretical predictions, which may lead to a potential risk of rebar fracture. Mechanics of load transfer on structures are explained as three main load paths and force transfer principles in the GSS region are further detailed.

In dynamic testing, the impact responses and failure processes of specimens are contrasted between the two connector categories. Subsequently, pull-out tests are performed on post-impact GSS connectors to reveal the failure modes and bond strength reduction percentages of post-damage couplers. The findings indicate that a structure with the top-of-footing connection exhibits a more ductile response and better impact resistance than those with a pier base connection. Based on the final failure patterns, most specimens maintain the GSS connection integrity and bond performance after impact loading, with major damage enacted as diagonal shear fractures occurring away from the GSS regions. Failure modes of post-impact couplers vary significantly with the connection type; GSS-F specimens show rebar tensile fractures near the coupler, while GSS-C specimens experience bond-slip failures at the narrow end. Moreover, GSS-F couplers exhibit minimal tensile capacity reduction (4% to 5%), demonstrating perfect bond integrity after impact, in contrast with GSS-C couplers, which show substantial tensile strength reductions of 10% and 98%.

This study not only provides novel and in-depth insights into theoretical research on the mechanisms of precast concrete construction utilizing a GSS system, but also contributes much-needed data from precast column impact tests and novel insights into residual bond strength analysis of post-impact GSS connectors.

# TABLE OF CONTENTS

# LIST OF TABLES

# LIST OF FIGURES

# EXECUTIVE SUMMARY

The objectives of this study are mainly twofold: 1) to investigate the material load-bearing percentages and force transmission rules of grouted in-static testing, and 2) to evaluate impact responses and failure processes of specimens under low-velocity impact and failure modes and bond strength reduction percentage of post-damage couplers in pull-out testing.

To carry out the first objective, precast concrete specimens with two different types of pier-footing connections are designed, cast, and tested under sequential compressive and lateral loads. The strain-time history at five critical areas on longitudinal reinforcements and GSSs are recorded and analyzed. The compressive and shear behaviors between the piers with couplers in the footing and those with connectors embedded in the pier base are then compared. Based on that, the recorded strains into loads based on the relative stiffness proportions of each material are converted and the load distribution percentage across the system are revealed. Experimental observations with the theoretical predictions are then compared. Finally, the compressive and shear load transmission mechanisms from a detailed model perspective are proposed.

The second objective is carried out by testing four precast concrete specimens with two categories of pier-footing connections under two different impacting velocities. Pull-out tests on post-impact GGS connectors are then conducted. The impact force-time relationships of the four specimens are recorded and analyzed. The strain-time history at five critical areas on longitudinal reinforcements and GSSs are then collected and compared. The failure processes and the crack propagation of specimens at four characteristic moments are observed and analyzed, and the final overall damage pattern and local damage at interface of specimens are identified. Regarding the pull-out test on post-impact couplers, the failure modes of post-impact couplers in two categories of GSS specimens are revealed. Finally, ultimate tensile stresses between post-impact and undamaged (healthy) couplers are compared to obtain a bond strength reduction percentage of damaged couplers after impact load.

Ultimately, the proposed load distribution and transmission principles can provide an in-depth understanding on the individual contributions of different materials and force transfer mechanisms in the coupler region, which is a foundational basis for ensuring effective bonding of the grout and enhancing the overall safety of bridge systems under various loading conditions.

Additionally, the dynamic response and failure modes of precast columns with GSS connectors can attain a comprehensive understanding of their impact resistance capacities. The investigation into the reduction of bond strength in post-impact GSS connectors is expected to provide the evaluation method of the damage levels in these couplers. These observations not only contribute valuable insights for calibrating and refining numerical models that simulate the GSS connections under dynamic loads but also offer a foundation for future bridge design to avoid potential damage from future impact events.

# 1. INTRODUCTION

## 1.1 Background

Compared to conventional cast-in-place (CIP) construction, accelerated bridge construction (ABC) is an innovative methodology where prefabricated bridge components are prepared off-site and then lifted, slid, or rotated into the connection for rapid assembly [1], [2], [3]. ABC can offer many remarkable advantages: 1) shorter construction and road closure time, 2) lower cost of new and replacement bridge construction, 3) less risk to workers and traveling public, 4) higher bridge element quality assurance, and 5) more environmentally friendly due to less energy consumption in construction [4]. Due to the benefits mentioned above and support from the Federal Highway Administration (FHWA), ABC has begun to be developed and implemented by many state DOTs, such as Utah, Massachusetts, and Washington State. Especially in Utah, many bridges have been built or replaced using ABC techniques such as the I-15 CORE Provo Center Street Interchange, the Riverdale Road over I-84, and the I-15 South Layton Interchange [5]. In May 2021, the Utah Department of Transportation (UDOT) scheduled a $122.7 million project to renew portions of two major highways (I-80 and I-215) in the Salt Lake Valley utilizing ABC [6].

To achieve capacity and structural system integrity, continuity of joints between precast bridge elements (e.g., prefabricated concrete deck panels, substructures, and superstructures) is particularly critical to resist the different forces acting on the structure. One type of connection is mechanical bar splices (MBS), commonly known as couplers, which establish a mechanical connection between two pieces of rebar inside the coupler by grout, threads, heads, and other mechanisms for meeting appropriate splice requirements [7]. There are five typical MBS in the market: 1) shear screw coupler, 2) headed bar coupler, 3) threaded coupler, 4) swaged coupler, and 5) grouted sleeve splice (GSS) coupler [8]. Compared with other couplers, the GSS is more widely adopted because it can provide easier installation and larger controllable construction tolerance. One type of GSS is shown in Figure 1.1 [9]. Two reinforcing bars extended from the two components are connected by high-strength grout pumped into a ductile iron sleeve after installation, and the tensile force is mainly transferred through bond between the rebar, grout, and sleeve.

In order to understand the mechanical behavior and failure modes of GSS connections, a number of scholars have carried out studies on the static response of the GSS's under the tensile and cyclic loading using different theoretical, experimental, and numerical methods [10, 11, 12]. However, none of them reflect the initial compressive stress state of the coupler or the critical influence of the surrounding concrete on the connector.

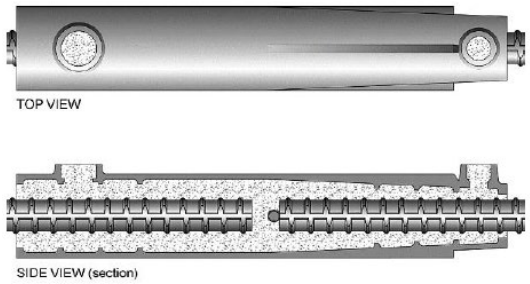


**Figure 1.1** Grouted sleeve splice (GSS) coupler [9]

During the design service life of 75 years, bridges inevitably experience a variety of loads from various natural (e.g., earthquake, flood, hurricane, landslide/debris flow, etc.) or human-caused hazards (e.g., vessel collision, vehicular collision, fire, explosion, etc.) [13]. Extreme disasters may cause not only severe damage or complete collapse of structures but economic loss and social disruption as well. The national seismic hazard map of the United States Geological Survey (USGS 2018) shows that peak ground accelerations in different regions have a 2% exceedance probability for various levels of seismic intensity in 50 years, as shown in Figure 1.2 [14]. In the moderate and high seismic zones, the reinforced concrete bridges are more susceptible to causing severe damage due to earthquakes. For providing seismic resistance, bridge piers should be designed by following significant criteria: lateral load capacity, displacement and rotation ductility capacity, and earthquake energy dissipation capacity. Regarding prefabricated bridges with connections, due to uncertain performance of couplers under seismic load, the couplers applied in plastic hinge parts of bridge piers are banned by U.S. codes in moderate and high seismic zones [15], [16], [17]. However, in October 2016, Utah DOT supported the application of grouted couplers in seismic zones.

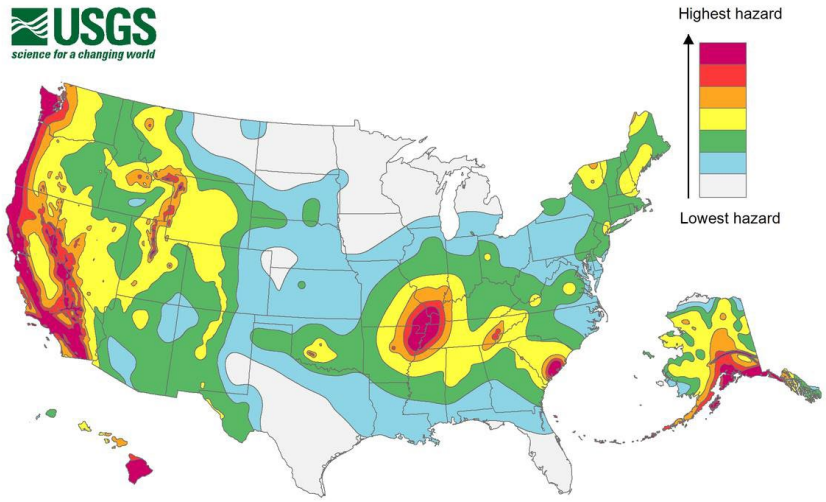


**Figure 1.2** National seismic hazard map [14]

With the popularization of ABC, the performance and understanding of the mechanical behaviors of precast bridge piers under earthquakes has also become increasingly crucial [18], [19], [20], [21], [22]. However, there is a noticeable gap in these studies when it comes to providing detailed explanations of the failure mechanisms and load transmission mechanisms within the GSS region under hazard conditions.

Excluding earthquakes, with the increasingly frequent occurrence of collision accidents, vessels and vehicles hit have become the third leading cause of bridge failures in the United States for the 39-year period between 1967 and 2006, accounting for 13% after flooding (hydraulic), as shown in Figure 1.3 [23]. As of 2012, bridge systems in 42 of the 50 states have suffered serious damage caused by truck collisions. Furthermore, 80% (40 of 50) of states have reported crashes resulting in minor bridge damage, and 60% (30 of 50) have reported minor scrapes resulting from vehicle collisions [24].

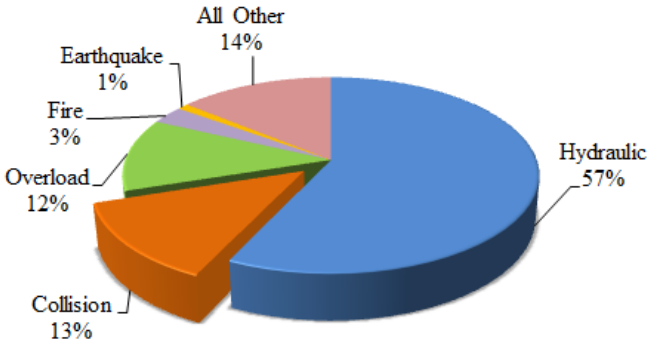


**Figure 1.3**:Causes of bridge failures [23]

Bridge piers, which are important load-bearing parts of structural systems, can suffer catastrophic failures due to vehicle crashes. Figure 1.4 shows the deadly impact crash by a tractor-trailer on the bridge support pier of Dolphin Road Overpass on I-30 in Dallas on 11 June 2012. As a result, the tractor-trailer was totally split in half and the top of easternmost pier failed due to shear failure [25]. Figure 1.5 shows a crash of semi-truck on a pier on northbound I-55, three miles south of Matthews, Missouri, on 27 September 2021. It resulted in one completely destroyed pier and another damaged pier [26]. In order to achieve bridge serviceability and capacity after crash incidents, much attention has been paid to impact load simplification, dynamic behavior of piers under vehicle collision, and damage assessment after impacting [27], [28], [29], [30], [31], [32], [33], [34]. In the current AASHTO-LRFD (2020) code, vehicular impact load is considered as a 2,700 kN (606.98 kips) equivalent static force applied to the height of 1.5 m (5.0 feet) above the ground level [13].

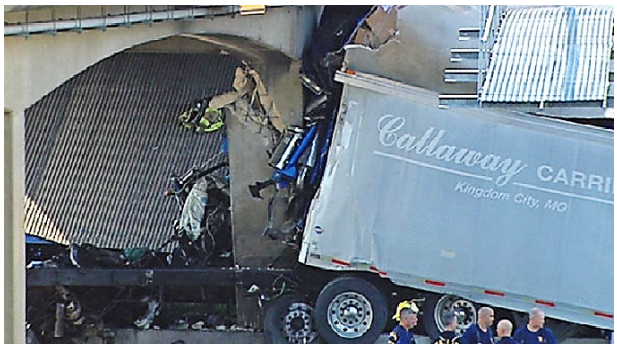


**Figure 1.4** Tractor-trailer collision on the I-30 Bridge, Texas (2012) [25]

**Figure 1.5** Semi-truck collision on the I-55 Bridge, Missouri (2021) [26]

Assessing the resilience of GSS connections subject to vehicular impact loads becomes critical for ensuring the structural safety of these bridges. There are limited studies that have conducted the dynamic analysis of precast concrete (PC) bridge pier with GSS connectors under impact loads [35], [36], [37]. However, the current studies are not sufficient to comprehensively explain the embedded locations' effect of GSS connectors on dynamic behavior and failure modes of precast columns under low-velocity impact loading, nor are they sufficient in providing available data to determine non-visible damage of the coupler system (i.e., coupler, rebar, and grout) under the same.

## 1.2 Problem Statement and Scope

Bridge systems are exposed to multiple extreme events, which are concurrent or a cascade of two or more hazards [38]. To illustrate the significance of this issue, consider a real-world scenario where a precast pier connected by GSSs is subjected to a vehicle collision at low velocity. While the pier's exterior might not display any obvious damage, microcracks may form within the sleeve, potentially reducing the coupler's connection capacity to effectively transfer future loads. This situation could threaten the integrity of the bridge system and reduce its residual capacity to withstand future hazardous loading conditions such as seismic rocking. Meanwhile, the bridge becomes vulnerable and exposes more potential risks in the occurrence of subsequent extreme events. Hence, it is necessary to understand in detail the load distribution in each material and load path principles in the coupler region. Furthermore, it is crucial to understand the failure mechanisms of precast columns and the residual bond strength of GSS connectors. This can form the foundational knowledge for ensuring the effective bonding of the coupler system and protecting the safety of precast piers against sequential hazards. However, to date, no study can be found that directly addresses this issue.

This research addresses the major gaps in the literature, which include the lack of test data and analysis of the compressive and shear behaviors of precast columns with GSS connectors. Moreover, this study provides much-needed data of impact testing of the precast columns with GSS connectors and residual bond strength analysis of the post-impact GSS connectors.

The specific research questions of this research are:

For static evaluations:

1) How do the strains change over time in key areas of longitudinal reinforcements and GSSs under sequential compressive and lateral loads, and how do these behaviors compare between different types of pier-footing connections?

2) How much load does each material carry, and how does this compare with theoretical predictions?
3) What are the compressive and shear force transmission mechanisms from a detailed model perspective?

For dynamic evaluations:

1) How do the impact forces change over time under two different impacting velocities, and how do these compare between different types of pier-footing connections?
2) How do strains change over time in key areas of longitudinal reinforcements and GSSs and how do these changes compare among the specimens?
3) How do cracks start and grow in these specimens during impacting?
4) What kind of damage can be observed both on the specimens' surface and at the interface between two parts of the concrete?
5) After pull-out tests, what kind of failure modes can be observed on post-impact couplers in two categories of GSS specimens?
6) Compared with undamaged (healthy) couplers, how much bond strength do the post-impact couplers retain?

## 1.3 Research Objectives

In order to answer the questions outlined in the previous section, the following outlines this study's research objectives.

For evaluating static behaviors, five precast concrete specimens with two different types of pier-footing connections are designed, cast, and tested under sequential compressive and lateral loads:

1) Record and analyze the strain-time history at five critical areas on longitudinal reinforcements and GSSs. Compare the compressive and shear behaviors between the piers with couplers in the footing and those with connectors embedded in the pier base.
2) Convert the recorded strains into loads based on the relative stiffness proportions of each material and reveal the load distribution percentage across the system, then compare experimental observations with the theoretical predictions.
3) Develop the compressive and shear load transmission mechanisms from a detailed model perspective.

For assessing dynamic performance, four precast concrete specimens with two categories of pier-footing connections are tested under two different impacting velocities. Pull-out tests on post-impact GGS connectors are then carried out:

1) Record and analyze the impact force-time relationships of the four specimens.
2) Collect and compare strain-time history at five critical areas on longitudinal reinforcements and GSSs.
3) Observe and analyze the failure processes and the crack propagation of specimens at four characteristic moments.
4) Identify the final overall damage pattern and local damage at interface of specimens.
5) Reveal the failure modes of post-impact couplers in two categories of GSS specimens.
6) Compare ultimate tensile stresses between post-impact and undamaged (healthy) couplers to obtain bond strength reduction percentage of damaged couplers after impact load.

Ultimately, the proposed load distribution and transmission principles can provide an in-depth understanding on the individual contributions of different materials and force transfer mechanisms in the coupler region, which is a foundational basis for ensuring effective bonding of the grout and enhancing the overall safety of bridge systems under various loading conditions.

Additionally, the dynamic response and failure modes of precast columns with GSS connectors can attain a comprehensive understanding of their impact resistance capacities. Investigating the reduction of bond strength in post-impact GSS connectors is expected to provide the evaluation method of the damage levels in these couplers. These observations not only contribute valuable insights for calibrating and refining numerical models that simulate the GSS connections under dynamic loads but also offer a foundation for future bridge design to avoid potential damage from future impact events.

## 1.4 Study Organization

This report is divided into six chapters. The introduction, Chapter 1, gives the general background, the problem statement and scope, and the objectives of the research study. Chapter 2 includes a literature review of current research relevant to this study. Chapter 3 presents an overview of the specimens and three test methodologies involving static tests to assess load distribution, dynamic tests to evaluate impact resistance, and pull-out tests to examine the bond integrity between reinforcing bars and connectors on post-impact GSSs. Chapter 4 contains static test results, load distribution conditions, and mechanics of compressive and lateral load transferring. Dynamic response and failure modes of precast concrete (PC) piers after impact testing are presented in Chapter 5; pull-out failure modes and reduction of bond strength in post-impact GSS connectors are also included. Chapter 6 ends the report with conclusions. A bibliography is shown at the end of the report.

# 2. LITERATURE REVIEW

Static testing of concrete structures typically includes tensile, compressive, flexural, and shear aspects to assess their performance under consistent conditions. Dynamic testing focuses on seismic tests to obtain the response under simulated seismic activity, impact tests to evaluate resilience against sudden impacts, fatigue tests to determine endurance fatigue stresses over the lifespan, and vibration tests to assess stability under scenarios such as traffic or machinery operation.

For the literature review, focusing on GSS associated static and dynamic studies between 2013 and 2024, two highly reputable databases, *Compendex* and *Web of Science,* are chosen. In addition, literature published in English and sourced from peer-reviewed journals are mainly collected. The search strategy involved a keyword string (“grouted splice sleeve” OR “grouted splice connection”) with static study types ("tensile", "compressive", "shear", and “flexural") and dynamic study types ("seismic"," impact"," fatigue", and" vibration"), respectively. The counts of articles for each category were recorded as Table 2.1. It reveals a significant interest in tensile and seismic tests, as indicated by the volume of literature found.

**Table 2.1** The counts of articles for each research category

| Database | | *Compendex* | *Web of Science* |
|---|---|---|---|
| static studies | “tensile” | 12 | 17 |
| | “compressive” | 2 | 3 |
| | “shear” | 7 | 9 |
| | “flexural” | 4 | 5 |
| dynamic studies | “seismic” | 25 | 29 |
| | “impact” | 5 | 3 |
| | “fatigue” | 2 | 2 |
| | “vibration” | 0 | 1 |

This literature review attempts to clarify and summarize current experimental research on tensile behavior of GSSs, and seismic and impact response of PC structures with GSSs. In existing studies, three primary testing methods are frequently utilized: pull-out tests for evaluating static tensile strength, push-over tests for seismic performance, and pendulum or drop hammer impact tests for resistance to dynamic impacts. This chapter aims to gather and synthesize these three experimental methods by qualitatively collecting failure modes and quantitatively analyzing the damage evaluation indices. This analysis helps to find gaps in the current research. It provides a basic insight into the testing of GSS connectors and serves as a reference for future experimental designs, and finally, producing unaddressed challenges for both static and dynamic areas.

## 2.1 Pull-out Testing

Pull-out testing is a direct method for measuring maximum tensile strength and identifying failure modes of GSS connections (i.e., coupler, rebar, and grout). Tensile force is mainly transferred through bonds between the rebar, grout, and sleeve. A pull-out testing machine includes a fixed part and a movable part, both of which clamp the ends of rebars, then apply a controlled tensile load or cyclic load on the moving end, as presented in Figure 2.1 (a). Throughout the testing process, the applied load and the displacement at the movable end are continuously monitored and recorded. Post-test analysis includes GSS failure modes, tensile strength of the GSS connection, and required anchorage length for the bond ability of GSSs.

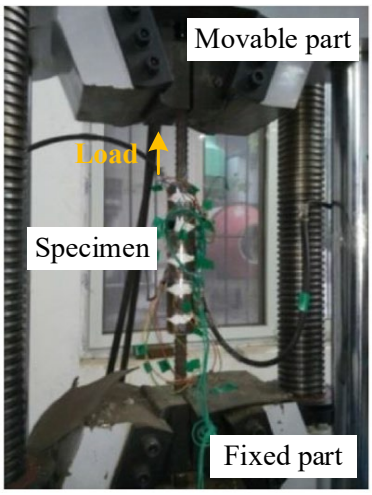


(a) Pull-out test [39]

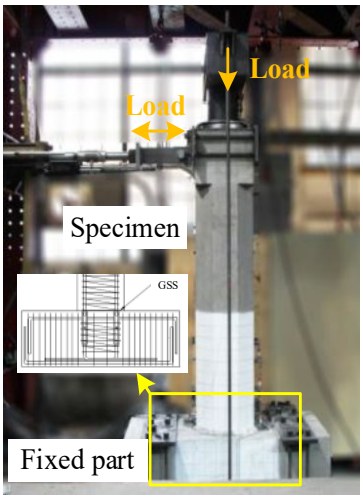


(b) Push-over test [40]

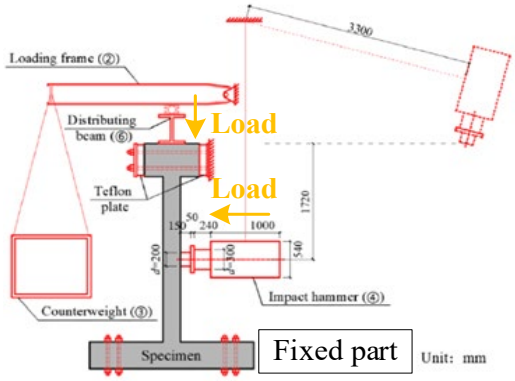


(c) Pendulum impact test [35]

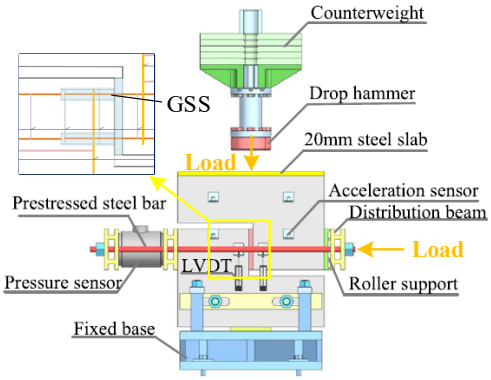


(d) Drop hammer impact test [36]

**Figure 2.1** Test setups and loading methods.

Pull-out tests were conducted on non-proprietary bar splice sleeve or commercial sleeve connectors, such as the NMB Splice Sleeve. These studies explored variables across three main components: bars (including embedded lengths and spliced bar diameters), sleeves (including sleeve diameters, sleeve lengths, and the presence of internal threads and wedges), and grout (specifically grouting defects), which are collected and shown in Table 2.2. These parameters were all found to influence the performance of GSS connectors. A notable finding was that increasing the diameter of the rebar, as well as the slope and length of wedges at both ends of the sleeve, and using threads within the sleeve, were all associated with increased tensile capacities [39] [41] [42]. Conversely, grouting defects can lead to a reduction in tensile strength [43] [44] [45].

**Table 2.2** Summary of pull-out tests on GSS connectors

| Reference | Specimens' geometry | Test information | Results | Remarks |
|---|---|---|---|---|
| Lu et al. (2019) [39] | **No. of tests:** 22<br>**Coupler type:** non-proprietary bar splice sleeve<br>**Coupler length:** 11.8-16 $d_b$<br>**Bar type:** yield strength 460 MPa (66.7 ksi)<br>**Bar size:** $\Phi$20 mm and $\Phi$22 mm | **Variables:** embedded lengths, spliced bar diameters and wedge lengths<br>**Load:** uniaxial tension | **Failure modes:** bar fracture, bond-slip failure<br>**Tensile strength:** 125% of yield strength of rebars<br>**Required anchorage length:** 6-6.4 $d_b$ | -The tensile capacity of the specimens increases with increasing diameter of the rebar and increasing slope and the wedge length at both ends of the sleeve. |
| Haber (2013) [46] | **No. of tests:** 9<br>**Coupler type:** NMB Splice Sleeve<br>**Coupler length:**14.6 $d_b$<br>**Bar type:** ASTM A615 Grade 60; yield strength 66.8 ksi<br>**Bar size:** No.8 ($\Phi$25 mm) | **Variables:** loading rate<br>**Loads:** uniaxial tension and cyclic loading | **Failure mode:** bar fracture<br>**Tensile strength:** 97.5% of tensile strength of rebars<br>**Required anchorage length:** N/A | - The increasing of loading rate does not affect the coupler performance.<br>-All failures are away from the coupler region. |
| Liu et al. (2020) [47] | **No. of tests:** 15<br>**Coupler type:** N/A<br>**Coupler length:** 18.5-20 $d_b$<br>**Bar type:** HRB400 yield strength 58 ksi<br>**Bar size:** $\Phi$14 mm, $\Phi$16 mm, $\Phi$18 mm, $\Phi$20 mm and $\Phi$22 mm | **Variables:** embedded lengths, spliced bar diameters, and sleeve diameters<br>**Load:** uniaxial tension | **Failure mode:** bar fracture<br>**Tensile strength:** equal with tensile strength of rebars<br>**Required anchorage length:** greater than 7 $d_b$ | -The significant grout fracture exists at the end of the sleeve. |
| Zheng et al. (2020) [43] | **No. of tests:** 24<br>**Coupler type:** N/A<br>**Coupler length:** 19.375 $d_b$<br>**Bar type:** HRB400 yield strength 58 ksi<br>**Bar size:** $\Phi$16 mm | **Variables:** insufficient grouting defects<br>**Loads:** uniaxial tension and cyclic loading | **Failure mode:** bar fracture, bond-slip failure<br>**Tensile strength:** 94%–116% of tensile strength of rebars<br>**Required anchorage length:** greater than 4 $d_b$ under uniaxial tension; greater than 5 $d_b$ under cyclic loading | -Compared with the fully grouted sleeve connection, defective sleeve connections have similar yielding and ultimate loads, but larger failure displacements. |
| Henin et al. (2015) [41] | **No. of tests:** 18<br>**Coupler type:** non-proprietary bar splice sleeve<br>**Coupler length:** 14.2–20 $d_b$<br>**Bar type:** ASTM A615 Grade 60; yield strength 66.8 ksi<br>**Bar size:** No.8 ($\Phi$25 mm), No.9 ($\Phi$ 28.7 mm) | **Variables:** sleeve lengths and spliced bar diameters<br>**Load:** uniaxial tension | **Failure mode:** bar fracture, bond-slip failure<br>**Tensile strength:** 99%–101% of tensile strength of rebars<br>**Required anchorage length:** around 7.5 $d_b$ | - Non-proprietary bar splice sleeves have fully capacity to develop reinforcing bars. |

| | | | | |
|---|---|---|---|---|
| Guo et al. (2022) [44] | **No. of tests:** 42<br>**Coupler type:** commercial sleeve connectors<br>**Coupler length:** 19.64 $d_b$<br>**Bar type:** HRB400 yield strength 58 ksi<br>**Bar size:** $\Phi$14 mm | **Variables:** multiple grouting defects<br>**Load:** uniaxial tension | **Failure mode:** bar fracture, bond-slip failure (failure of top bar, and failure of bottom bar)<br>**Tensile strength:** 65%–101% of tensile strength of rebars<br>**Required anchorage length:** 70 mm (5 $d_b$) | -The decrease of the total effective anchor lengths of bars changes the failure mode from bar fracture to bond-slip failure. |
| Li et al. (2022) [42] | **No. of tests:** 30<br>**Coupler type:** non-proprietary bar splice sleeve<br>**Coupler length:** 17.67 $d_b$<br>**Bar type:** HRB400 yield strength 58 ksi<br>**Bar size:** $\Phi$12 mm | **Variables:** the internal threads size, the wedges slope, and the embedment lengths<br>**Loads:** uniaxial tension and cyclic loading | **Failure mode:** bar fracture, bond-slip failure<br>**Tensile strength:** 44%–105% of tensile strength of rebars<br>**Required anchorage length:** greater than 7 $d_b$ | -Using threads and wedges can improve the tensile strength of sleeves. |
| Zhang et al. (2022) [45] | **No. of tests:** 7<br>**Coupler type:** N/A<br>**Coupler length:** 18.4-19.3 $d_b$<br>**Bar type:** HRB400 yield strength 58 ksi<br>**Bar size:** $\Phi$18 mm, $\Phi$20 mm, $\Phi$22 mm and $\Phi$25 mm | **Variables:** grout compactness<br>**Load:** uniaxial tension | **Failure mode:** bar fracture, bond-slip failure<br>**Tensile strength:** 50%–102% of tensile strength of rebars<br>**Required anchorage length:** N/A | - The decrease of grout compactness changes the failure mode from bar fracture to bond-slip failure. |

Notes: $d_b$ is diameter of rebar.

### 2.1.1 Failure Modes of GSS Connectors

Two typical failure modes of the GSS specimens were observed across the studies: (a) rebar fracture failure, and (b) bond-slip failure, as shown in Figure 2.2. In general, the tensile capacity of the connection mainly depends on the tensile strength of the rebar and the bonding strength generated between the rebar and the grout material. Rebar fracture failure occurs when the bond strength within the coupler exceeds the ultimate tensile strength of the rebar, leading to rebar fracture before any bond failure. This indicates that bars reach or surpass their tensile capacity before failure, demonstrating effective connection behavior of the connecting sleeve. In general, bond-slip failures happen when the bond strength within the coupler falls below the ultimate tensile strength of the rebar, resulting in bond failure before rebar fracture. This indicates an ineffective GSS connection that may affect load transfer efficiency and structural integrity.

The shift in failure mode from bar fracture to bond-slip failure is primarily attributed to the anchorage length [44]. Due to grouting defects, the anchorage length may be insufficient to ensure adequate bond capacity between the grout and bar.

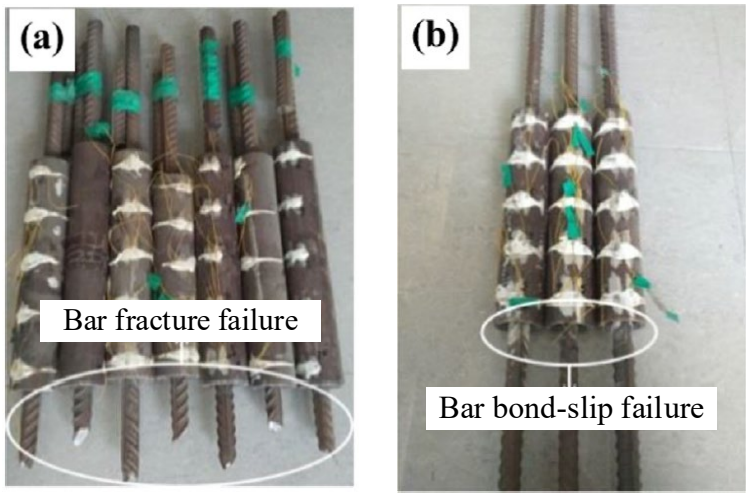


(a) Bar fracture (b) Bond-slip failure

**Figure 2.2** Failure modes of GSS connectors [39]

## 2.1.2 Evaluation on Single GSS Connector

### *2.1.2.1 Required anchorage length*

Rebar anchorage length is defined as a region where the rebar is effectively engaged with the surrounding grout to transfer load. When the rebar anchorage length exceeds the requirement length, the GSS shows perfect connecting behavior, preventing slippage between grout and rebar. Conversely, if the anchorage length is smaller than the requirements, the connection via the sleeve becomes inefficient. This inadequate connection is due to a reduced number of ribs on the steel bar's surface and a smaller contact area between the rebar and the grout, leading to bond-slip failures. By determining the necessary anchorage length, engineers can utilize materials efficiently, ensuring that the GSS is both safe and economical.

After collecting the required anchorage lengths from various studies, it is evident that the required anchorage length under uniaxial tension varies by different research findings. In uniaxial tension tests, the required anchorage lengths range from 4 $d_b$ to greater than 7 $d_b$, as shown as Table 2.3. The majority of the studies indicate that an anchorage length greater than 6 $d_b$ is often required to ensure satisfactory performance. Specifically, Zheng et al. (2020) presents a notably lowest required anchorage length (greater than 4 $d_b$ for uniaxial tension and greater than 5 $d_b$ for cyclic loading) [43], while Guo et al. (2022) identify a minimum requirement of 5 $d_b$ [44]. The significantly shorter required anchorage lengths are attributed to test variables with the effects of ground defects on anchorage lengths in studies [44], in contrast to others that focus on the rebar and sleeve's geometric parameters.

**Table 2.3** Summary of required anchorage length

| Reference | Load | Required anchorage length |
|---|---|---|
| Lu et al. (2019) [39] | uniaxial tension | 6–6.4 $d_b$ |
| Liu et al. (2020) [47] | uniaxial tension | greater than 7 $d_b$ |
| Zheng et al. (2020) [43] | uniaxial tension | greater than 4 $d_b$ |
| | cyclic loading | greater than 5 $d_b$ |
| Henin et al. (2015) [41] | uniaxial tension | around 7.5 $d_b$ |
| Guo et al. (2022) [44] | uniaxial tension | 5 $d_b$ |
| Li et al. (2022) [42] | uniaxial tension | greater than 7 $d_b$ |
| | cyclic loading | |

### *2.1.2.2 Tensile strength*

According to Section 5.11.5.2.2 of the current AASHTO (American Association of State Highway and Transportation Officials) LRFD Bridge Design Specifications, it requires that all mechanical reinforcing splices must develop at least 125% of the specified yield strength of the rebar [13]. In a summary of the literature, the tensile strength of the GSS specimens varied significantly, from the lowest of 44% to the highest of 125% of the yield strength of the rebars, as presented in Table 2.4 and Figure 2.3.

In Figure 2.3, Lu et al. (2019) achieved the AASHTO requirement, demonstrating that GSS connectors can significantly enhance the load-bearing capacity of the spliced bars beyond their nominal strengths, indicating GSS's ability to maintain structural integrity and safety [39]. However, most of the studies presented ranges or values below AASHTO requirements, with percentages varying from 94% to 116% of the rebar's yield strength. Despite not meeting code standards, these GSSs still retain more than 90% of the rebar's tensile strength. It means systems might perform adequately under designed loads, while the structures may not offer desired safety against the immediate risks. Guo et al. (2022), Li et al. (2022), and Zhang et al. (2022) reported even lower ranges, with the minimum values ranging from 44% to 65% [44]. Such connections might not be able to support normally designed loads, posing a serious risk to the system's ability to maintain structural integrity.

**Table 2.4** Summary of tensile strength of GSSs

| Reference | Percentage of rebar tensile strength |
|---|---|
| Lu et al. (2019) [39] | 125% |
| Haber (2013) [46] | 97.5% |
| Liu et al. (2020) [47] | 100% |
| Zheng et al. (2020) [43] | 94%–116% |
| Henin et al. (2015) [41] | 99%–101% |
| Guo et al. (2022) [44] | 65%–101% |
| Li et al. (2022) [42] | 44%–105% |
| Zhang et al. (2022) [45] | 50%–102% |

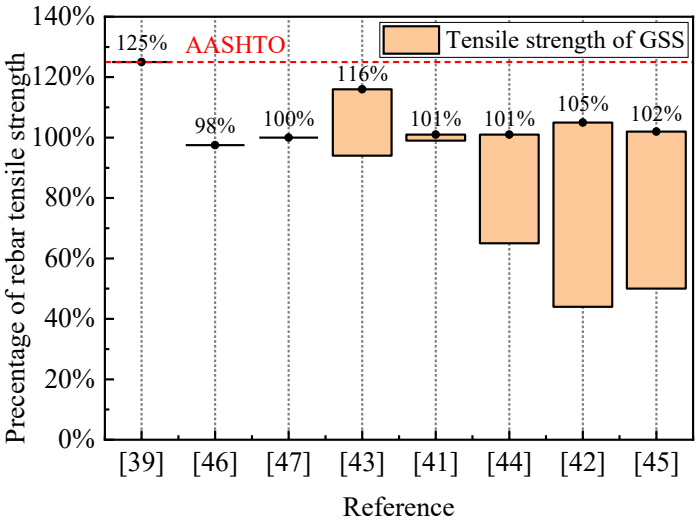


**Figure 2.3** Summary of tensile strength of GSSs

### 2.1.3 Gaps in Current Pull-out Tests

As the connections in footing-pier assemblies, embedded GSSs are subjected to compressive loading due to the gravity and service loads transferred from pier and other superstructure components. Furthermore, the connection's composite section includes four different materials: concrete, grout, the cast iron connector, and rebar. Therefore, the contribution of the surrounding concrete on the grouted sleeve connection cannot be neglected in the complex load transfer process. Overall, the current studies on tensile behavior of single GSS connections are insufficient as do not reflect the initial compressive stress state of the coupler or the critical influence of the surrounding concrete on the connector. However, this test offers a valuable perspective to evaluate the tensile capacity reduction through testing couplers post-impact in comparison with those in a healthy situation.

## 2.2 Push-over Testing

The push-over test is an essential part to assess seismic performance and determine failure modes under earthquake conditions. Displacement ductility capacity refers to the structure's ability to perform significant deformation beyond its yield point without failing. High ductility is crucial for seismic resilience, allowing structures to absorb and dissipate energy during an earthquake. In a push-over test, a column-footing assembly is secured on a strong floor or within a rigid testing frame. While the footing part is fixed, loads are applied at the top of column in two directions. In the vertical direction, compressive load is applied to simulate gravity load and other service loads typically acting on a bridge column. Furthermore, a lateral load is applied horizontally and increased gradually for simulating the lateral forces experienced during an earthquake, as shown in Figure 2.1 (b). During the testing, both lateral load and the displacement are captured. After analyzing these collected data, several key performance indicators can be identified, such as stiffness degradation, displacement ductility capacity, energy dissipation capacity, and plastic rotation capacity. Post-test failure modes are also observed.

A number of push-over tests were carried out on half-scale column-to-footing joints embedded with NMB Splice Sleeve or commercial sleeve connectors. These studies explored and investigated the influence of variables such as coupler location (either in-column or in-footing), the deboned region location, and the presence of features like pedestals or central tenons on seismic performance of the columns, which are summarized as Table 2.5.

Notably, the location of GSS connectors and deboned region significantly affect the columns' seismic performance. Columns with GSSs in footings exhibited a more ductile response and better energy dissipation capacity, but less seismic resilience compared to specimens with couplers in columns [40]. In addition, proper placement of a deboned region, such as an 8-inch deboned section in the footing or below the interface, causes a positive effect on the seismic performance of specimens [48] [49]. However, improperly deboned region position, like two 4-inch deboned sections above and below the interface, respectively, negatively affect the structure's seismic behavior [49]. Moreover, the use of pedestal can reduce the displacement capacity of the columns [46], while the presence of tenon improves the columns' seismic performance [50].

**Table 2.5** Summary of push-over tests on PC columns with GSS connectors

| Reference | Specimens' geometry | Test information | Results | Remarks |
|---|---|---|---|---|
| Pantelides et al. (2017) [40] | **No. of columns:** 3<br>**Scale Factor:** 50%<br>**Column section:** octagonal diameter 21 in. (533 mm)<br>**Coupler type:** NMB Splice Sleeve<br>**Connection type:** column-to-footing<br>**Coupler length:** 14.6 $d_b$<br>**Bar type:** ASTM A615 Grade 60; yield strength 66.8 ksi<br>**Long. bar size:** 6 No.8 ($\Phi$25 mm) | **Variables:** coupler location<br>**Loads:** axial compression load on vertical direction and cyclic quasi-static displacement in lateral direction | **Failure modes:** cracks, spalling, fractured rebar, and exposed rebar cage.<br>**Displacement ductility:** 8.9 (CIP), 5.4 (couplers in column). 6.1 (couplers in footing) | -Compared to specimens with couplers in columns, those with GSSs in footings exhibited a more ductile response and better energy dissipation capacity but less seismic resilience. |
| Ameli et al. (2017) [48] | **No. of columns:** 3<br>**Scale Factor:** 50%<br>**Column section:** octagonal diameter 21 in. (533 mm)<br>**Coupler type:** NMB Splice Sleeve<br>**Connection type:** column-to-footing<br>**Coupler length:** 14.6 $d_b$<br>**Bar type:** ASTM A615 Grade 60; yield strength 66.8 ksi<br>**Long. bar size:** 6 No.8 ($\Phi$25 mm) | **Variables:** coupler location and deboned region location<br>**Loads:** axial compression load on vertical direction and cyclic quasi-static displacement in lateral direction | **Failure modes:** cracks, spalling, fractured rebar, and exposed rebar cage.<br>**Displacement ductility:** 8.9 (CIP), 6.8 (couplers in column with 8-in. [203 mm] deboned region in footing), 6.1 (couplers in footing) | - Compared to the performance of the CIP specimen, both PC specimens have more ductile performance. |
| Barton et al. (2022) [49] | **No. of columns:** 2<br>**Scale Factor:** 50%<br>**Column section:** octagonal diameter 21 in. (533 mm)<br>**Coupler type:** NMB Splice Sleeve<br>**Connection type:** column-to-footing<br>**Coupler length:** 14.6 $d_b$<br>**Bar type:** ASTM A615 Grade 60; yield strength 66.8 ksi<br>**Long. bar size:** 6 No.8 ($\Phi$25 mm) | **Variables:** deboned region location<br>**Loads:** axial compression load on vertical direction and cyclic quasi-static displacement in lateral direction | **Failure modes:** cracks, spalling, fractured rebar, and exposed rebar cage.<br>**Displacement ductility:** 7.5 (couplers in footing with 8-in. [203 mm] deboned region below the interface), 5.4 (couplers in footing with two 4-in. [102 mm] deboned region above and below the interface, respectively) | - 8 $d_b$ debonding of column longitudinal steel bars causes a positive effect on the seismic performance of specimens. |

| | | | | |
|---|---|---|---|---|
| Tazarv (2014) [51] | **No. of columns:** 1<br>**Scale Factor:** 50%<br>**Column section:** circular diameter 24 in. (610 mm)<br>**Coupler type:** NMB Splice Sleeve<br>**Connection type:** in column above a pedestal<br>**Coupler length:** 14.6 $d_b$<br>**Bar type:** ASTM A615 Grade 60; yield strength 66.8 ksi<br>**Long. bar size:** 11 No.8 ($\Phi$25 mm) | **Variables:** N/A<br>**Loads:** axial compression load on vertical direction and cyclic quasi-static displacement in lateral direction | **Failure modes:** cracks, spalling, fractured rebar, and exposed rebar cage.<br>**Displacement ductility:** 7.07 | -Precast specimen shows the same seismic performance with CIP specimen. |
| Haber (2013) [46] | **No. of columns:** 3<br>**Scale Factor:** 50%<br>**Column section:** circular diameter 24 in. (610 mm)<br>**Coupler type:** NMB Splice Sleeve<br>**Connection type:** in column<br>**Coupler length:** 14.6 $d_b$<br>**Bar type:** ASTM A615 Grade 60; yield strength 66.8 ksi<br>**Long. bar size:** 11 No.8 ($\Phi$25 mm) | **Variables:** with pedestal or without pedestal<br>**Loads:** axial compression load on vertical direction and cyclic quasi-static displacement in lateral direction | **Failure modes:** cracks, spalling, fractured rebar, and exposed rebar cage.<br>**Displacement ductility:** 7.36 (CIP), 4.52 (couplers in column above pedestal), 4.53 (couplers in column above footing) | - Two precast specimens show 40% lower displacement capacity compared with CIP specimen. |
| Liu et al. (2022) [50] | **No. of columns:** 3<br>**Scale Factor:** 50%<br>**Column section:** square (500 mm x 550 mm)<br>**Coupler type:** N/A<br>**Connection type:** in column<br>**Coupler length:** 20 $d_b$<br>**Bar type:** HRB400 yield strength 58 ksi<br>**Long. bar size:** 14 $\Phi$16 mm | **Variables:** with central tenon or without tenon<br>**Loads:** axial compression load on vertical direction and cyclic quasi-static displacement in lateral direction | **Failure modes:** cracks, spalling, fractured rebar, and exposed rebar cage.<br>**Displacement ductility:** 3.95 (CIP), 3.57 (GSS), 4.54 (GSS with tenon) | -The using of tenon improves the seismic performance of column |

Notes: Long. bar is the longitudinal bars, which are connected by GSS.

### 2.2.1 Failure Modes on PC Columns

In the synthesis of reviews, four typical failure modes of the PC specimens were observed during the failure processes: (a) cracks, (b) spalling, (c) exposed rebar cage, and (d) fractured rebar, as shown in Figure 2.4. Unlike the failure modes of GSS connectors, these failure modes happen sequentially, offering a clear progression of structural damage. For a detailed introduction, an experimental observation from reference is selected and clarified [40] as follows: (a) Cracks: the testing began with a minor hairline crack at the bed grout at the column-to-footing interface. This initial crack widened over time, with a new crack appearing just above the GSS connectors. As the testing continued, major cracks developed, including a significant crack at the bed grout, another near the top of the GSS connectors, and a third within the spiral-overlapping zone approximately 30 inches above the column base. (b) Spalling: spalling was first observed near the corners of the octagonal column, starting with an area height of about 4 inches on both sides of the column.

Spalling increased in severity, particularly around the GSS connectors, with the spalled area and crack width expanding as the testing advanced. The spalling exposed deeper areas of the column, especially over the GSS connectors. (c) Exposed rebar cage: the damage progression led to the exposure of the rebar cage, particularly noted in the later testing stages. The spiral reinforcement and GSS connectors became visible through the spalled concrete, highlighting the extent of material degradation and structural damage. (d) Fractured rebar: the final and most severe stage of damage involved the fracturing of rebar, attributed to low cycle fatigue. These fractures occurred just below the surface of the footing in areas devoid of confining transverse reinforcement, representing a critical point of structural failure.

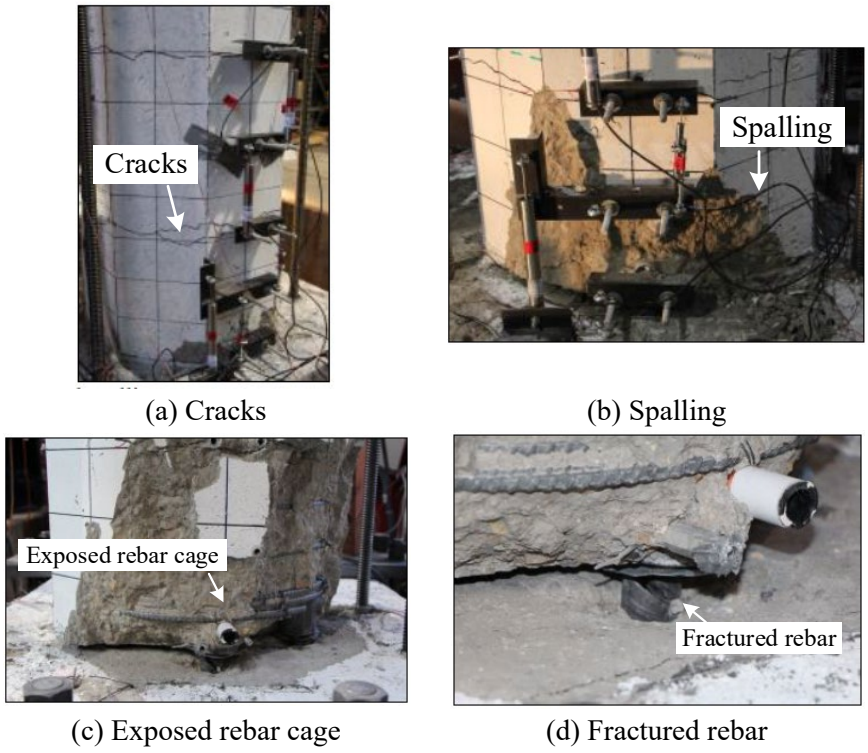


(a) Cracks (b) Spalling

(c) Exposed rebar cage (d) Fractured rebar

**Figure 2.4** Failure modes of PC columns in push-over tests [40]

## 2.2.2 Evaluation on PC Columns under Seismic Load

### *2.2.2.1 Displacement ductility*

Displacement ductility is a measure of how much a structure or a structural component can deform plastically after yielding. It is calculated as the ratio of the ultimate displacement (the maximum displacement a structure can withstand before failure) to the yield displacement (the displacement at which a structure first yields). It is a crucial indicator of the seismic resilience of bridge piers, while higher displacement ductility values indicate that a structure can absorb and dissipate more energy during earthquakes.

Various studies on displacement ductility are compared in Table 2.6. It reveals that ductility values are influenced by several factors, including construction methods (CIP vs. PC methods), coupler location (either in-column or in-footing), the deboned region location, and the presence of features like pedestals or central tenons. Pantelides et al. [40], Ameli et al. [48] and Haber [46] report that CIP columns exhibit higher displacement ductility, with reports of 8.9 and 7.36, indicating the better seismic resilience compared with PC columns. The coupler location significantly influences displacement ductility; the structure with footing couplers shows higher ductility (6.1) compared with the one with column-located

couplers (5.4) [40]. For the structures with deboned regions, Barton et al. demonstrate how the placement and size of deboned regions can affect ductility, with values ranging from 5.4 to 7.5, which can either enhance or reduce ductility depending on their features [49]. Furthermore, the use of tenons in structures improves displacement ductility from 3.57 (GSS) to 4.54 (GSS with tenon) [50].

**Table 2.6** Summary of displacement ductility

| Reference | Displacement ductility | Column feature |
|---|---|---|
| Pantelides et al. (2017) [40] | 8.9 | CIP |
| | 5.4 | couplers in column |
| | 6.1 | couplers in footing |
| Ameli et al. (2017) [48] | 8.9 | CIP |
| | 6.8 | couplers in column with 8-in. [203 mm] deboned region in footing |
| | 6.1 | couplers in footing |
| Barton et al. (2022) [49] | 7.5 | couplers in footing with 8-in. [203 mm] deboned region below the interface |
| | 5.4 | couplers in footing with two 4-in. [102 mm] deboned region above and below the interface, respectively |
| Tazarv (2014) [51] | 7.07 | couplers in column above a pedestal |
| Haber (2013) [46] | 7.36 | CIP |
| | 4.52 | couplers in column above pedestal |
| | 4.53 | couplers in column above footing |
| Liu et al. (2022) [50] | 3.95 | CIP |
| | 3.57 | GSS |
| | 4.54 | GSS with tenon |

#### *2.2.2.2 Plastic rotation capacity*

Plastic rotation capacity is an ability to undergo large deformations beyond the elastic limit without losing its load-carrying capacity. It is the difference between the ultimate rotation and the yield rotation obtained from bending moment-rotation plots of a test specimen. Higher plastic rotation capacity indicates higher ductility of the structure, meaning it can sustain significant deformations without losing its ability to support loads. They have better seismic performance and more resilience during an earthquake.

Pantelides et al. plotted the relationships of the plastic rotation (rad)-moment (ft-kip) for each test specimen [40]. Barton et al. demonstrated that a specimen with couplers in footing, with an 8-in. deboned region below the interface, exhibited a better plastic rotation capacity compared with that of two 4-in. deboned regions above and below the interface [49].

#### *2.2.2.3 Energy dissipation capacity*

Energy dissipation capacity refers to the capability to absorb and dissipate the energy input during an earthquake, reducing the energy transferred to other parts of structure. Hysteresis loops, which are the relationships between load and deformation in the form of a loop, are recorded and plotted after testing. The area enclosed by the hysteresis loops is referred to as the hysteretic energy of a system. The energy dissipation capability is a key performance indicator in seismic design, directly impacting a structure's ability to survive in seismic events.

Pantelides et al. stated that both the CIP column and that with footing coupler had a slightly better energy dissipated performance than the precast pier with column coupler [40]. Barton et al. revealed the hysteretic energy dissipation of specimens with couplers in the footing; one with an 8-in. deboned region below the interface was 1.30 times of the CIP specimen. However, another with couplers in the footing, with two 4-in. deboned regions above and below the interface, showed 90% hysteretic energy dissipation of the CIP specimen [49]. In exploring the energy dissipation capacity between CIP piers and pier embedded GSS and central tenon connections, Liu et al. presented that pier embedded GSS and central tenon can significantly increase energy dissipation capacity of PC piers [50].

#### *2.2.2.4 Stiffness degradation*

The degradation of stiffness over time or number of cycles can be expressed as the ratio of the stiffness at any given cycle to the initial stiffness, or by plotting this ratio against the number of cycles to visually represent the degradation process. A higher stiffness degradation indicates a greater reduction in the structure's ability to resist deformation under seismic loading.

Pantelides et al. indicated that the inclusion of GGS connectors at the base of columns did not significantly affect the rate of stiffness degradation observed throughout the seismic testing. Furthermore, it was found that columns integrated with a footing coupler demonstrated a slightly greater average stiffness at every drift ratio [40]. This increase in stiffness is primarily attributed to the higher lateral force capacity of the precast structure.

### 2.2.3 Gaps in Current Push-over Testing

Generally, the existing research focus is on presenting the overall or local damage pattern under cyclic pushover load. However, there is a noticeable gap in these studies when it comes to providing detailed explanations of the failure mechanisms and load transmission mechanisms within the GSS region under hazardous conditions. Addressing this knowledge gap is crucial for ensuring the structural integrity and resilience of ABC bridge systems.

## 2.3 Pendulum or Drop Hammer Impact Testing

The pendulum impact test particularly simulates the effect of dynamic impacts or sudden forceful events, such as vehicular collisions. This test aims to evaluate the impact performance and failure modes of PC columns. Similar to the push-over test, the footing portion is fixed and the vertical compressive load is applied on the top of column. For the impact, a pendulum's mass is initially hoisted and then released to strike the column for simulating realistic scenarios, as shown in Figure 2.1 (c). During the testing, lateral load and the displacement are monitored. By analyzing the lateral displacement-time relationship, the maximum lateral displacement is determined, showing the column's resistance capacity under the impact forces. The failure modes are observed after the test.

The drop hammer impact test is a conventional method for simulating the effect of impact loads on structures. In this test, specimens are typically positioned horizontally, with the bottom side of the specimen fixed on the base directly below the drop hammer. A weight, typically made of steel, is designed to be dropped from a controlled height. A steel plate is placed at the top surface of the test specimen to prevent local damage due to impact loading, as shown in Figure 2.1 (d). During the testing, impact force and the displacement are recorded. The failure process and failure pattern are observed during the test. A summary of impact tests on PC structures with GSS connectors is shown as Table 2.7.

**Table 2.7** Summary of impact tests on PC structures with GSS connectors

| Reference | Specimens' geometry | Test information | Results | Remarks |
|---|---|---|---|---|
| Zhou et al. (2022) [35] | **No. of columns:** 1<br>**Scale Factor:** N/A<br>**Column section:** square (250 mm x 250 mm)<br>**Coupler type:** commercial sleeve connectors<br>**Connection type:** in column<br>**Coupler length:** 20 $d_b$<br>**Bar type:** HRB400 yield strength 58 ksi<br>**Long. bar size:** 4 $\Phi$18 mm | **Variables:** N/A<br>**Loads:** axial compression load in vertical direction and impact load in lateral direction | **Failure modes:** cracks, spalling, and bond-slip failure<br>**Maximum lateral displacement:** 135.6 mm | - Diagonal cracks mainly develop in the top side of the columns. -Cracks also occurred at bottom of columns. |
| Sun et al. (2022) [36] | **No. of specimens:** 1<br>**Scale Factor:** N/A<br>**Specimen section:** square (200 mm x 200 mm)<br>**Coupler type:** half grouted sleeve connectors<br>**Connection type:** N/A<br>**Coupler length:** 11.67 $d_b$<br>**Bar type:** HRB400 yield strength 58 ksi<br>**Long. bar size:** 4 $\Phi$12 mm | **Variables:** N/A<br>**Loads:** axial compression load in horizontal direction and impact load in vertical direction | **Failure modes:** shear cracks and bar shear fracture | - The crack mainly occurred at the interface on upper L-shaped component during the entire impact process.<br>- No evident damage was observed in the lower L-shaped component where GSS was installed. |

### 2.3.1 Failure Modes on PC Columns

The pendulum impact test shows bond-slip failures within the sleeve connectors and narrow cracks at the grout outlet and the sleeve's midsection, indicating slippage of the steel bars within the connector, as shown in Figure 2.5 (a) [35]. In contrast, the drop hammer test exhibits a bar shear fracture. This is attributed to shear failure being the principal mechanism of damage in these scenarios, as illustrated in Figure 2.5 (b) [36].

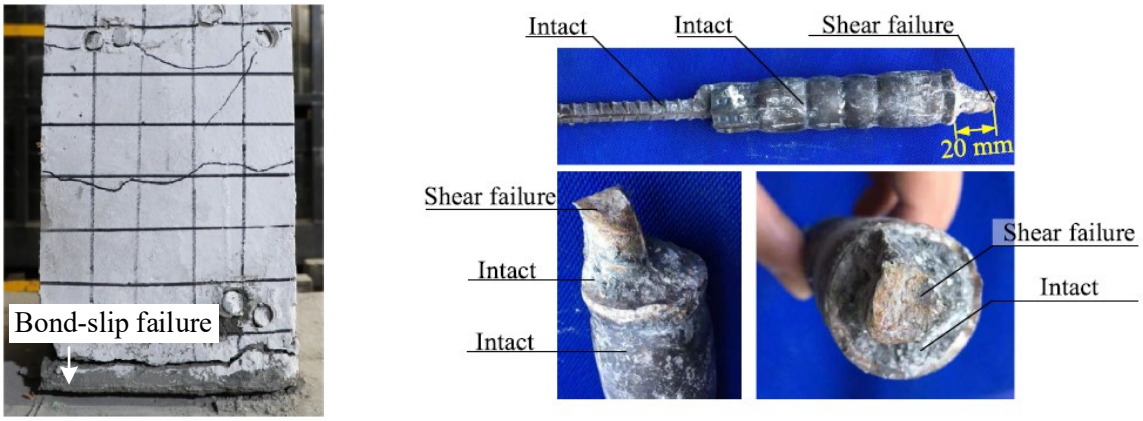


(a) Bond-slip failure [35] (b) Bar shear fracture [36]

**Figure 2.5** Failure modes in impact testing

### 2.3.2 Evaluation on PC Columns under Impact Load

#### *2.3.2.1 Maximum lateral displacement*

Similar to displacement ductility, maximum lateral displacement is a key factor to assess the dynamic behavior of PC columns. It refers to the largest horizontal movement experienced by a structure or its components due to external forces, helping engineers design structures that can withstand potential lateral forces without failing. Zhou et al. reported that specimens equipped with GSS connections achieved a maximum lateral displacement of 135.6 mm, then used them to compare GSS connection performance with other types of structural connections, assessing their anti-impact capacity [35].

### 2.3.3 Gaps in Current Impact Testing

There are limited studies that have conducted the dynamic analysis of PC bridge piers with GSS connectors under impact loads. The current studies are insufficient to comprehensively explain the embedded locations' effect of GSS connectors on dynamic behavior and failure modes of precast columns under low-velocity impact loading. The are also insufficient in providing available data to determine non-visible damage of the coupler system (i.e., coupler, rebar, and grout) under the same impact loading.

## 2.4 Summary

This chapter provides a comprehensive literature review of relevant research and studies, gathering three primary testing methods utilized frequently: pull-out tests for evaluating static tensile strength, push-over tests for seismic performance, and pendulum or drop hammer impact tests for resistance to dynamic impacts. The chapter began with a brief overview of searching strategy on static and dynamic studies about GSS connectors, revealing a significant research interest in tensile and seismic tests.

A detailed summary of test methods and post-test analyses of pull-out testing are provided, including GSS failure modes, tensile strength of the GSS connections, and required anchorage length for the bond ability of GSSs. A number of scholars have studied the static response of the GSSs under tensile and cyclic loading, exploring variables across three main components: bars, sleeves, and grout. However, none of them reflect the initial compressive stress state of the coupler or the critical influence of the surrounding concrete on the connector.

To assess seismic performance and determine failure modes under earthquake conditions, most of the studies have focused on post-test failure modes of the PC column and four key performance indicators: stiffness degradation, displacement ductility capacity, energy dissipation capacity, and plastic rotation capacity. A few studies provide detailed explanations of the failure mechanisms and load transmission mechanisms within the GSS region under earthquake conditions.

Two pendulum and drop hammer impact tests were introduced at the chapter's end. Only limited studies that have conducted the dynamic analysis of PC bridge piers with GSS connectors under impact loads can be found in the databases. Obviously, the current studies are insufficient to comprehensively explain the embedded locations' effect of GSS connectors on dynamic behavior and failure modes of precast columns under low-velocity impact loading; nor are they sufficient in providing available data to determine non-visible damage of the coupler system (i.e., coupler, rebar and grout) under the same.

This research addresses the literature's major gaps, which are the lack of load distribution in each material, a detailed aspect of load path principles in the coupler region, failure mechanisms of precast columns, and the residual bond strength of GSS connectors. Moreover, this study contributes in-depth understanding on the individual contributions of different materials and force transfer mechanisms in the coupler region, which is a foundational basis for ensuring effective bonding of the grout and enhancing the overall safety of bridge systems under various loading conditions. Additionally, it provides much-needed data regarding impact tests of the precast columns with GSS connectors and the evaluation method of the reduction of bond strength in post-impact GSSs.

# 3. TEST METHODOLOGIES

To evaluate the static and dynamic performance of pier-to-footing joints utilizing grout splice sleeve (GSS) connectors, cylindrical sections of bridge piers and foundations are selected as specimens of the study. This section covers an overview of the specimens, including their general information, the used material properties, and the processes in preparing the specimens. Following this, three tests are designed and carried out: static tests to assess load distribution, dynamic tests to evaluate impact resistance, and pull-out tests to examine the bond integrity between reinforcing bars and connectors on post-impact GSSs.

## 3.1 General Information of Test Specimens

For pier-to-footing joints, GSS connectors are commonly embedded in the pier base or in the footing top, as shown in Figure 3.1. The first pier-to-footing joint category is designated as GSS-F, which is composed of a precast column with protruded 7-inch dowel bars and a precast footing with connectors embedded in the top of the footing. Alternatively, the GSS-C specimen is similarly comprised of a PC pier and footing but locates the coupler in the column base and connects to 7-inch dowels protruding from the footing top. Considering the influence of the surrounding concrete on the GSS connector, the section of bridge piers and foundations are selected as study specimens, which include cylindrical PC pier and precast footing with an 8-inch diameter connected by a single GSS on longitudinal rebars.

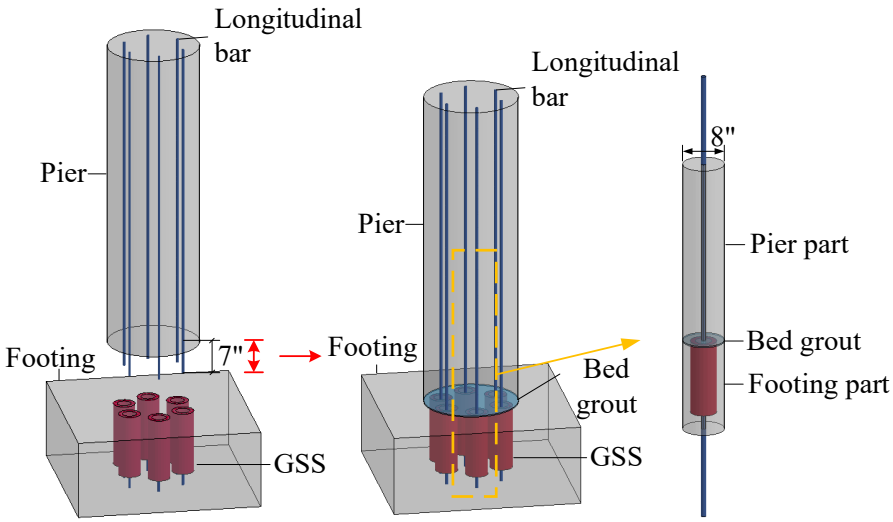


(a) GSS-F

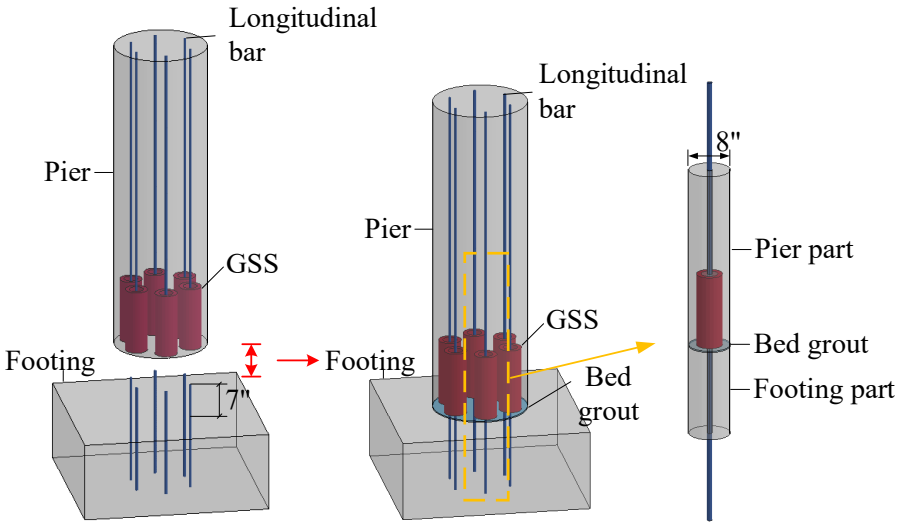


(b) GSS-C

**Figure 3.1** Details of pier-to-footing joints

In total, five pier-footing connections are constructed and tested: three precast GSS-F specimens and two precast GSS-C specimens. One specimen from GSS-F is treated as a control pretest case, which is used to verify the testing and data acquiring methodology. The remaining four specimens are then used to collect the data. To simplify the naming, the two GSS-F specimens are named F1, F2, while the two GSS-C specimens are labeled C1 and C2.

For each joint, the pier portion has a circular cross-section with an 8-inch diameter and an overall height of 36 inches. The footing part has the same cross-sectional geometry as the pier and a total length of 18 inches. The longitudinal steel reinforcements of all specimens are No. 8 ASTM A615 reinforcing bars (diameter = 1 inch) with 18 inches left on both sides. Figure 3.2 (a) and (b) show the reinforcing bars' details and dimensions of the test specimens. The commercially available grout-filled sleeves (NMB Splice Sleeve) are used to connect the longitudinal bars in the pier and footing. The GSS has a wide end and a narrower end with multiple internal ribs and two grout injection ports. The internal ribs contribute to the mechanical interlock with grout, thereby increasing the bond strength of couplers. Meanwhile, the rebar stop is implemented to ensure the proper embedment length of the reinforcing bars. In constructing the precast components, the GSS is typically cast in one of the prefabricated components, where the reinforcing bars are inserted into the narrow open end. Steel bars protrude from the other precast part for embedding the wide end of the coupler because this end provides more tolerance space to embed rebars. The type 8U-X NMB Splice Sleeve is recommended and typically used for No. 8 rebar. Geometrical details of the GSS are shown in Figure 3.2 (c).

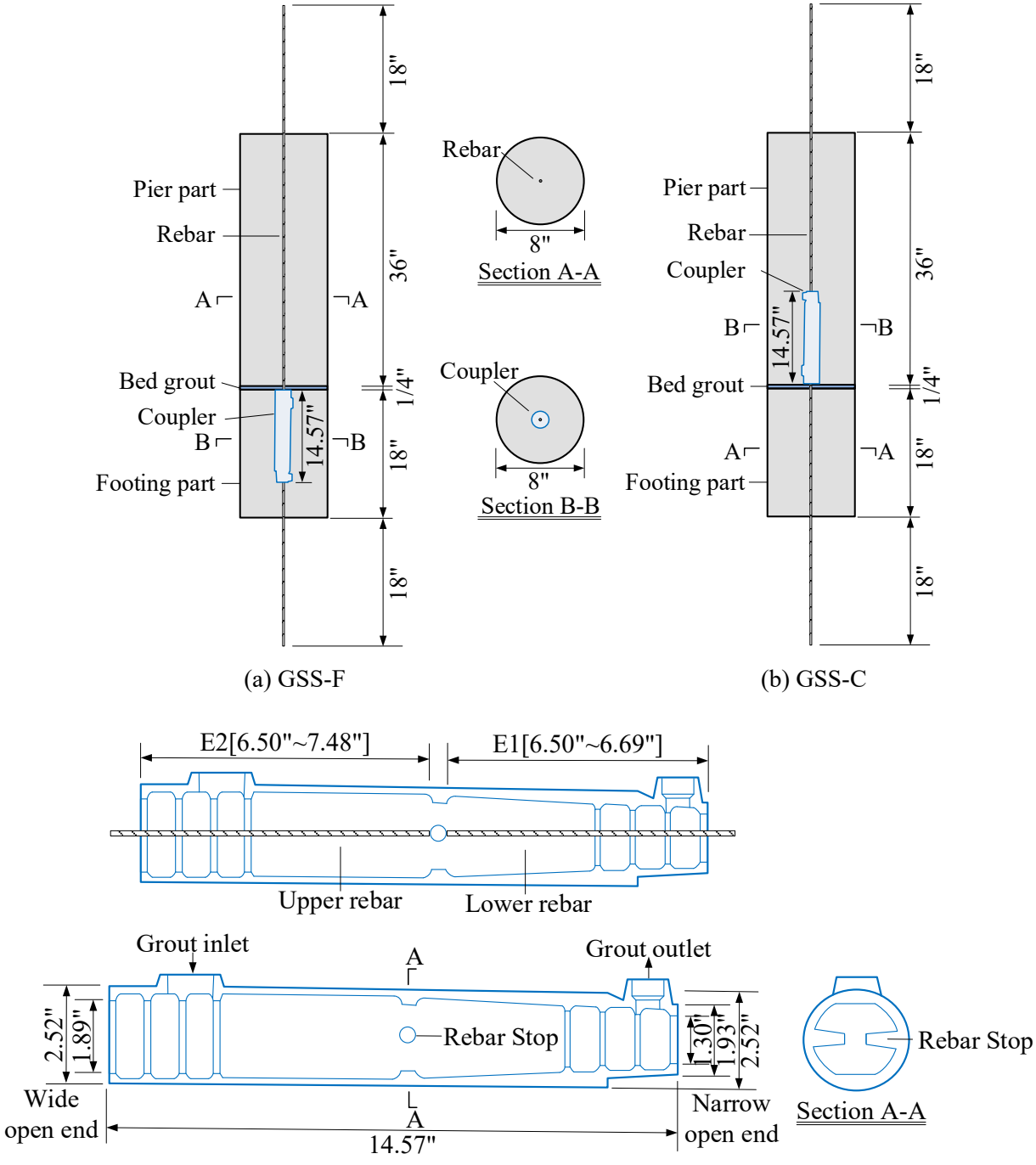


(a) GSS-F

(b) GSS-C

(c) Grout splice sleeve

**Figure 3.2** Dimensions and GSS specimen details (unit: inch)

## 3.2 Material Properties

The Type U-X sleeves are iron castings conforming to specification ASTM A536-84 [52], with a grade of 85-60-06. Steel reinforcement is ASTM A615 grade 60 steel. Table 3.1 illustrates the mechanical properties of the GSS and reinforcements, including tensile strength, yield strength, and elastic modulus. To acquire the compressive strength of concrete before removing the specimens from the formworks based on ASTM C39 [53], six 4 in. x 8 in. concrete cylinders are prepared and tested using a Tinius Olsen testing machine at a standard curing period of 28 days and the test day, respectively. Additionally, six 2-inch cubes are cast to obtain the compressive strength of the grout at a full 28-day curing period and the test day in accordance with ASTM C109 [54]. The average and the standard deviation of concrete and grout compressive strengths are presented in Table 3.2. Compression test details are shown in Figure 3.3.

According to the ACI 318 (08) Code [55], the modulus of elasticity of concrete ($E_c$) is calculated using the following equations:

$$E_c = 57{,}000\sqrt{f_c'}\ \text{psi} \qquad \text{For } f_c' < 6000\ \text{psi}$$
$$E_c = \left(40{,}000\sqrt{f_c'} + 1.0\times10^6\right)(w_c/145)^{1.5}\ \text{psi} \qquad \text{For } f_c' = 6000\sim12000\ \text{psi} \qquad \text{Eq. 1}$$

Where: $w_c$ is the density of grout in pounds per cubic foot (pcf) and $f_c$' represents the compressive cylinder strength in psi. In the calculations of $E_c$, the normal weight of grout is taken as 125 pcf. The compressive strengths of concrete and grout are directly sourced from the average values at test day in Table 3.2. The calculated moduli of elasticity are also presented in Table 3.2.

**Table 3.1** Material properties of reinforcement and coupler

| Type | GSS | Rebar |
|---|---|---|
| Grade | 85-60-06 | 60 |
| Minimum yield strength $f_y$ (ksi/MPa) | 60 ksi/414MPa | 60 ksi/414MPa |
| Minimum tensile strength $f_u$ (ksi/MPa) | 85 ksi/586MPa | 90 ksi/621MPa |
| Modulus of elasticity $E$ (ksi/GPa) | 24,400 ksi/168 GPa | 29,000 ksi/200 GPa |

**Table 3.2** Material properties of concrete and grout

| Specimen | | 4 in. × 8 in. concrete cylinders | 2-in. grout cubes |
|---|---|---|---|
| Water-material ratio | | 0.45 | 0.148 |
| Modulus of elasticity $E_c$(ksi/GPa) | | 4,400 ksi/30.3 GPa | 4,300 ksi/29.6 GPa |
| 28-day (ksi/MPa) | Average compressive strength | 5.8 ksi/39.99 MPa | 11.5 ksi/79.29 MPa |
| | Standard deviation | 0.51 ksi/3.5 MPa | 0.95 ksi/6.5 MPa |
| Test-day (ksi/MPa) | Average compressive strength | 6.0 ksi/41.37 MPa | 11.8 ksi/81.36 MPa |
| | Standard deviation | 0.61 ksi/4.2 MPa | 0.56 ksi/3.9 MPa |

(a) Tinius Olsen compression machine

(b) 4 in. × 8 in. cylinder

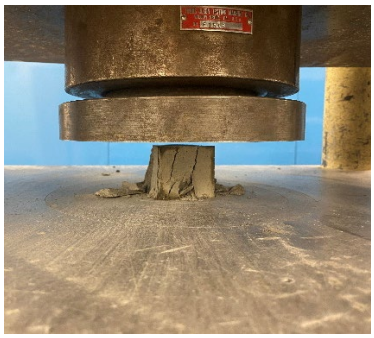

(c) 2-in. cube

**Figure 3.3** Details of compression test

## 3.3 Preparation of Specimens

As the plastic hinge region and the connection area are typically the most susceptible to damage under lateral seismic and vehicle impact loads [36], [48], five strain gauges are installed in these critical areas. Specifically, these gauges are adhered to the reinforcements at the top of the pier (S1), the reinforcement at the exiting ends of the coupler (S3 & S5), the middle section of the coupler (S4), and the end of coupler adjacent to the bed grout (S2), as shown in Figure 3.4.

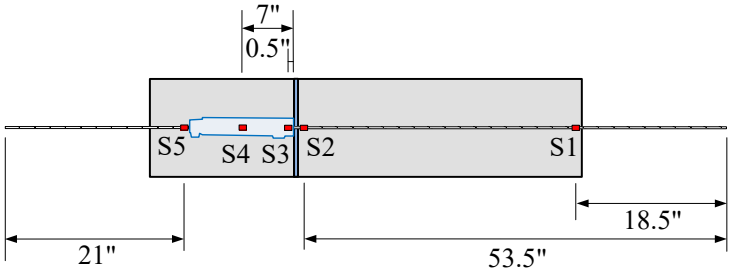


(a) GSS-F

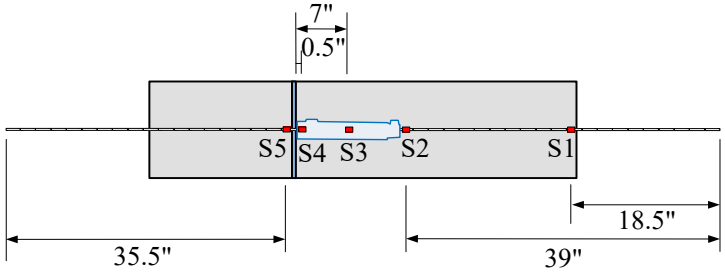


(b) GSS-C

**Figure 3.4** Strain gauge placement

Figure 3.5 presents the construction procedures of the precast specimen that consists of five main steps: (1) C2A-06-125LW-120 gauges (with a resistance value of 120 ohms) are bonded to the prepared surfaces. To protect the strain gauges and their associated wires from potential moisture in concrete, M-Coat B and protective tape are applied to the strain gauges, while their wires are carefully encased inside the hollow PVC tubing. (2) Each cylindrical formwork is composed of an 8-inch-diameter Sonotube, a 10-inch square wood sheet, and 2-inch-wide wood strip. For GSS-F, to ensure that couplers remained

hollow after concrete casting, rubber plugs with diameters of ¾ inch and 1 inch are made for sealing the grout outlet and inlet holes, respectively. For GSS-C, for making sure the grout pathways of outlet and inlet are clear, PVC pipes with the same diameters as plugs are inserted in both holes and held by the Sonotube. (3) The mixed concrete is then poured into the formworks. After the cylinders' average compressive strength reaches 6 ksi, the specimens are removed from their formworks. (4) A 55-lb. bag of SS Mortar is sufficiently mixed with one gallon (8.34 lbs.) of water using an electric mixer with an NMB paddle, maintaining an average speed of 850 rpm for three minutes. Five 1/2-inch-wide circular frames are cut from the Sonotubes to provide molds for pouring the bed grout. (5) All the pier parts are lifted by a laboratory crane to around 1/2 feet above the corresponding footing. Considering the different locations of couplers, two distinct methods are utilized for the GSSs' grouting. For GSS-F, both the coupler and bed connection on the footing are filled with prepared grout using a grout pump (see Figure 3.5.c). Subsequently, the column is gently lowered, ensuring that it is placed vertically at the footing top. Alternatively, for GSS-C, the bed connection area is first filled with grout and the pier is then lowered into the right position. Afterward, the mixed grout is pumped into the wide end port of the sleeves by utilizing the grout pump until the grout flowed from top opening, which demonstrates that the coupler is completely filled. Both openings are sealed with tape once the grout has time to cure. It is important to note that all grouting operations are carried out within 40 minutes after mixing. Once the grout has attained sufficient strength, the temporary circular frames are removed.

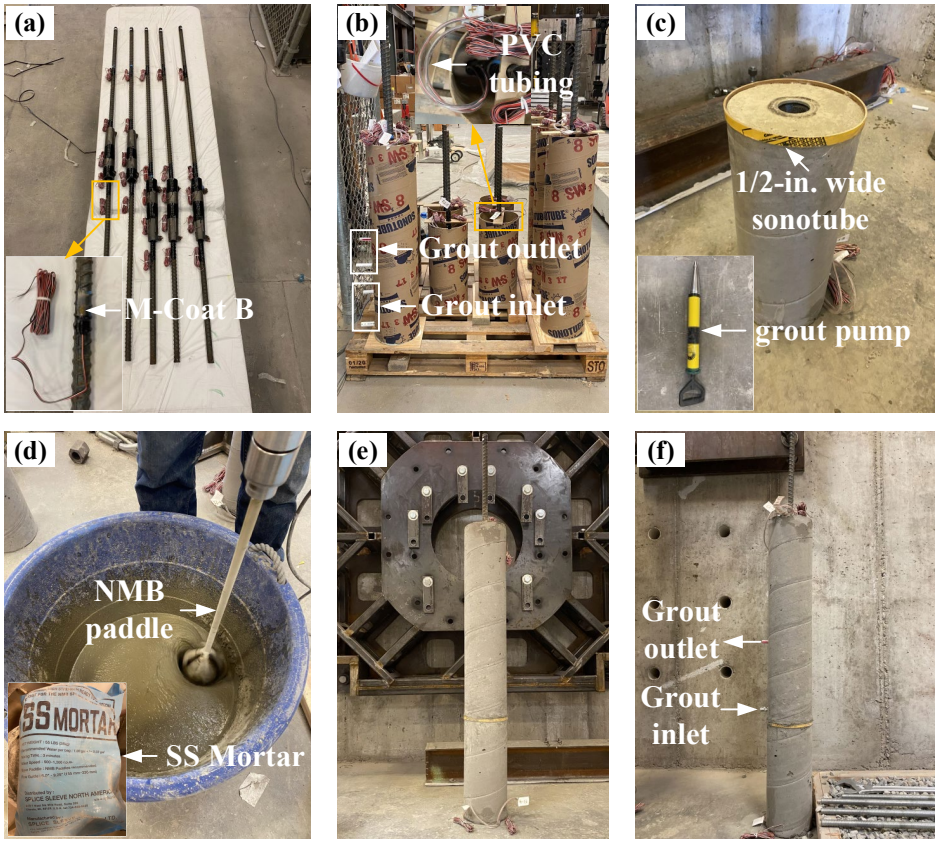


**Figure 3.5** Construction procedures of specimens: (a) attachment of strain gauges, (b) formwork of cylinders, (c) formwork of bed grout, (d) grouting preparation, (e) GSS-F assembly, (f) GSS-C assembly

## 3.4 Static Test Setup and Loading

Exploring load distribution in multiple material sections and load path principles in the coupler region, this section presents the methodology on the static tests on specimens with GGS connectors under sequential compressive and lateral loads.

In this experiment, specimens are placed horizontally inside a steel frame that provides rigid constraints in both horizontal and vertical directions, as shown in Figure 3.6. The axial load application system is comprised of a cylindrical hydraulic jack with a load capacity of 120 kips, a load cell, three concrete-filled steel tube (CFST) blocks that are used to transfer the reaction force from the frame, and several steel plates for distributing the load uniformly across the tested element and reducing localized stresses. Note that these blocks and plates feature 1.5-inch diameter central holes to accommodate the pass-through of the rebars. The lateral loading system includes an MTS actuator with a 5-inch displacement range and a 120-kip maximum load capacity, a load cell, a cylinder for load transfer, and multiple steel plates. To replicate the actual boundary conditions of a bridge pier, three steel bearings are positioned: one under the left side of the footing part, one at the left side of the footing-column interface, and one under the right side of the pier part, as shown in Figure 3.6 (a.2). In addition, to prevent the footing portion from flexural deformation during the lateral loading stage, a longitudinal plate with the same length as the footing portion and a transverse steel plate with anchor holes on both sides are sequentially placed on the specimens. Two high-strength steel rods are secured using top and bottom plates, which are bolted to the top transverse plate and the bottom base ground, respectively.


(1) (2)

(a) Pictures of test setup

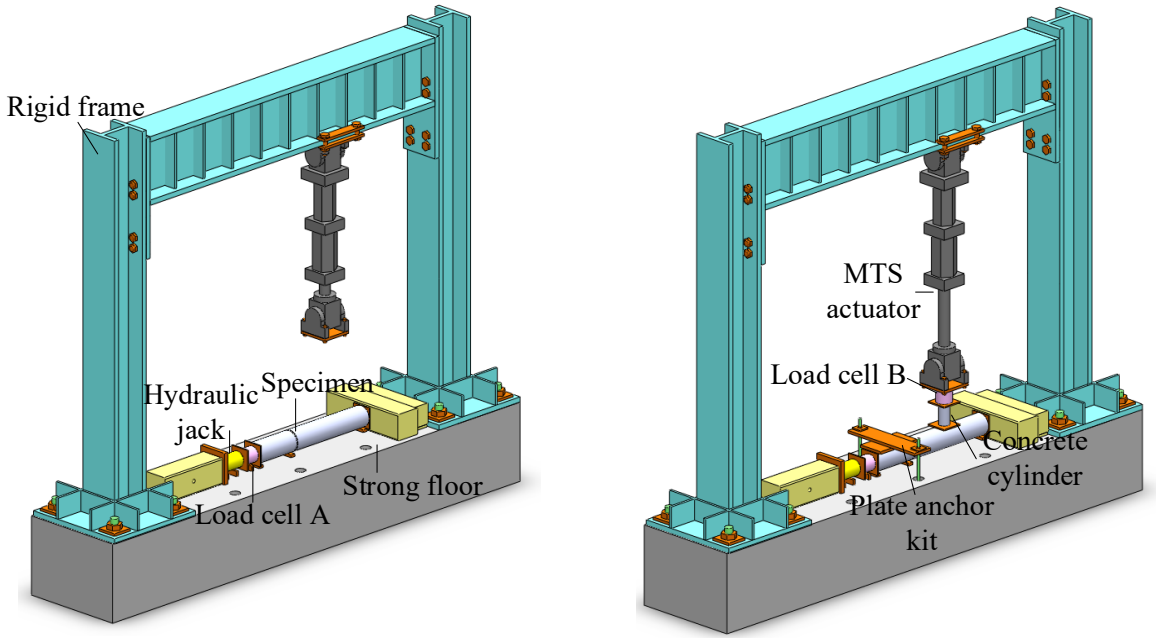


(1) (2)

(b) Schematic setup overviews

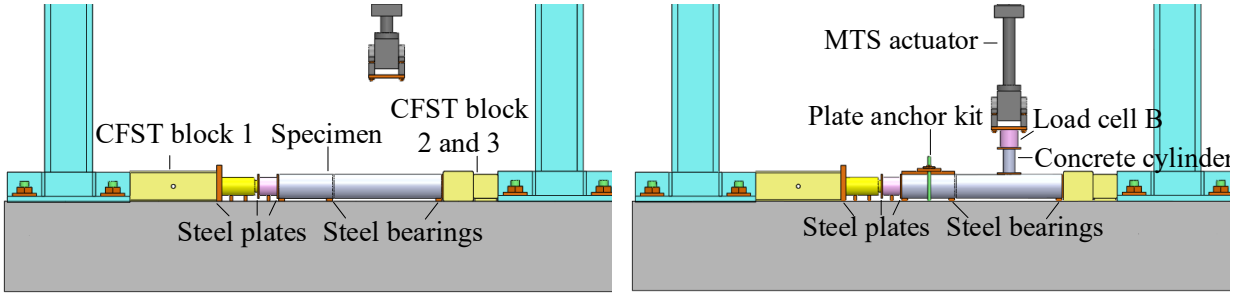


(1) (2)

(c) Schematic setup front views

**Figure 3.6** Static test setup: (1) axial compression loading stage; (2) multi-step lateral ramp loading stage

The entire loading procedure is divided into two stages: (1) Axial compression loading—to simulate the gravity load typically present in a bridge column, an axial compressive load, equivalent to 10% of the column axial capacity (30 kips) is applied. The load rate is set to 0.5 kips/s until the end of the 30-kip load, and the load is maintained at this constant for the duration of the test. (2) Multi-step lateral ramp loading—the maximum lateral point load is determined by assuming the extreme fiber stress under the combined axial and bending load reaches the strength capacity of concrete. The loading function is applied at the midpoint of the pier section by the MTS actuator at three stages of 20% (2 kips), 30% (3 kips), and 50% (5 kips) of the maximum lateral point load. The load is applied at a rate of 0.2 kips/s. Upon reaching each load stage, the load is maintained for a five-second duration. The specific loading protocols for each specimen are shown in Figure 3.7. During the test, strain data from both the reinforcements and the grouted sleeves, as well as load data of the axial compressive and ramped loads, are recorded at a frequency of 2.5 readings/second (2.5HZ) using a CS datalogger and BDI data

acquisition system, respectively. The actual loads measured by load cell A and B are plotted and shown in Figure 3.7. They show that, although maintaining a consistent loading rate is challenging, the applied static loads closely matched the prescribed design loads.

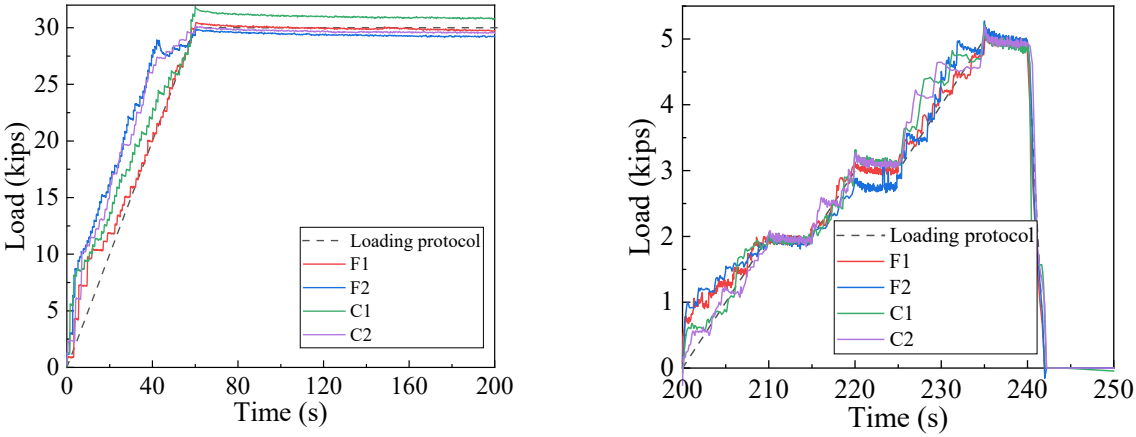


(a) Axial compression load time history (b) Multi-step lateral ramp load time history

**Figure 3.7** Loading protocols and actual loads

## 3.5 Dynamic Test Setup and Loading

Evaluating the lateral impact resistance of GSS connectors is essential to ensure the overall safety of precast structures under unexpected impact loads. This section presents the methodology of the low-velocity impact tests on specimens with GGS connectors to assess their dynamic behavior and identify damage patterns.

In this experiment, specimens are placed horizontally on the concrete floor. Axial compression load and impact load are subsequently applied in horizontal and vertical directions, as shown in Figure 3.8. Generally, these two-direction constraints are provided by the steel rigid frame fixed on the strong floor. To simulate the gravity load typically presented in a bridge column, a consistent axial compressive load, equivalent to 10% of the column axial capacity (30 kips), is first applied with loading rate of 0.5 kips/second by a cylindrical hydraulic jack. On one side of the jack, a load cell is placed to observe and record the axial load. In addition, three concrete-filled steel tube (CFST) blocks and several steel plates, with 1.5-inch diameter central holes, are located between the frame and specimen to distribute and transfer the load.

Regarding the vertical restriction and loading system, three steel bearings and a kit of bolted plates are used to replicate the real-world boundary conditions of the footing part. The loading system includes an MTS actuator at the midpoint of the pier section with a 5-inch displacement range and a 120-kip maximum capacity, a load cell, a steel cube for load transfer, and multiple steel plates. The actuator is programmed as displacement control, starting from an initial position of -2 in. (indicating no load applied) and moving at a constant load rate until the maximum displacement of -4.6 in. is achieved. Finally, the actuator returns to the initial position at the same velocity. To explore the behavior of the GSS precast column under varying impact conditions, two impact velocities, 0.5 in./second and 2 in./second are carried out in these tests. The displacement control protocols are shown in Figure 3.9. During the test, strain data from both the rebars and the grouted sleeves are recorded at a frequency of 5 readings/second (5HZ) using a CS datalogger, and the impact force is automatically collected by the MTS system.

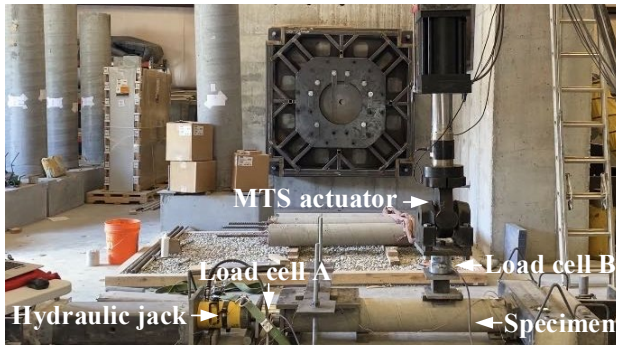


(a) Pictures of test setup

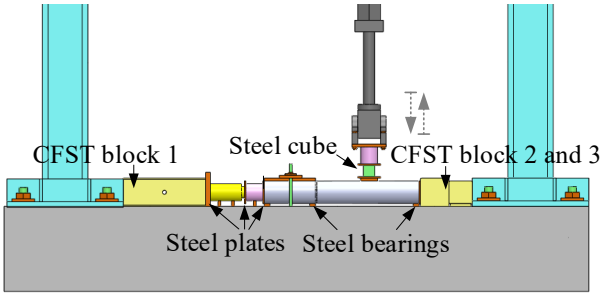


(b) Schematic setup front view

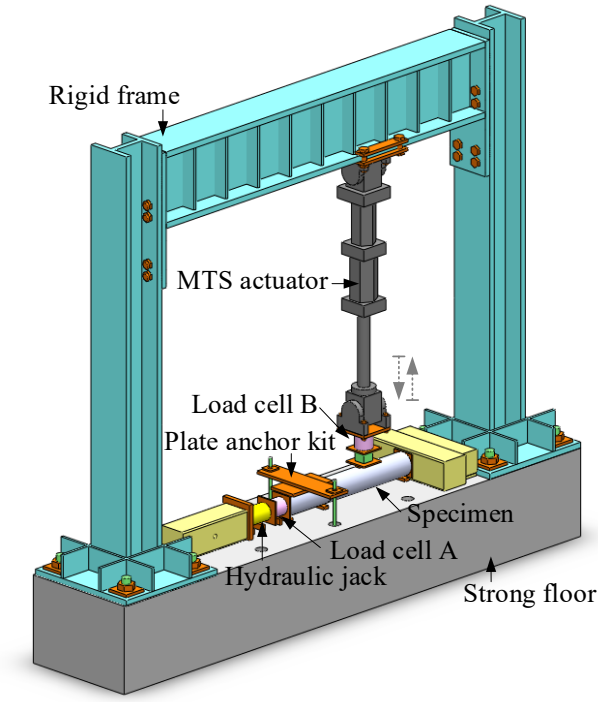


(c) Schematic setup overview

**Figure 3.8** Dynamic test setup

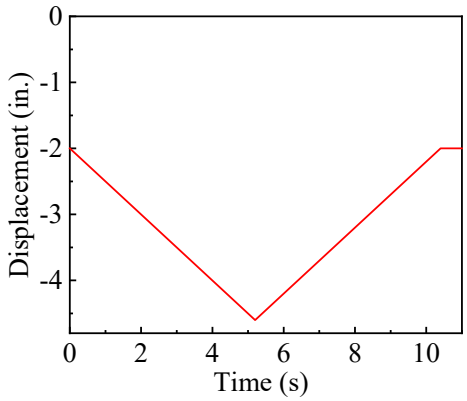


(a) For F1 and C1 (impact velocity=0.5 in./s)

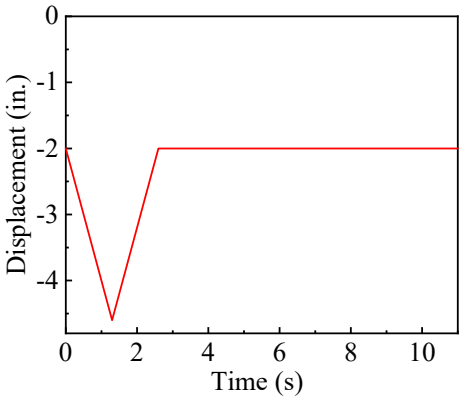


(b) For F2 and C2 (impact velocity=2 in./s)

**Figure 3.9** Displacement control protocols of the MTS actuator

## 3.6 Pull-out Test Setup and Loading

Pull-out testing is not only a direct method for assessing the bond integrity between the reinforcing bar and the coupler, but also can reveal the bond strength reduction and the residual tensile capacity of GSS connectors after impact loading.

After impact loading, the concrete cover is broken up and removed from the coupler and bonded rebars. Care is taken to cautiously remove the concrete without damaging the bond between the coupler and rebar. For fitting the GSS system to the pull-out test machine, the ends of the rebars are cut down to 10 inches outside of the coupler, as shown in Figure 3.10 (a). To prevent the grout from cracking due to cutting vibrations, the rebar area being cut is securely clamped during this process. The coupler specimens are then loaded in increasing tension using a Tinius Olsen testing machine, as shown in Figure 3.10 (b). The testing setup involves fixing the two rebar ends at 4 inches using steel tapper anchors with ribs, where only the upper beam is allowed movement to apply the load. Four tests are carried out under displacement control with a displacement rate of 0.2 in./min. [47]. During the test, both the load and displacement data are automatically recorded. To determine the standard strain-stress relationships from measured displacement-load data, strain of the GSS system is calculated by dividing the displacement of the upper beam by the length of coupler region (coupler length plus 8 in.). Bar stress is obtained by dividing the tension load by the area of the rebar (0.79 in.$^2$).

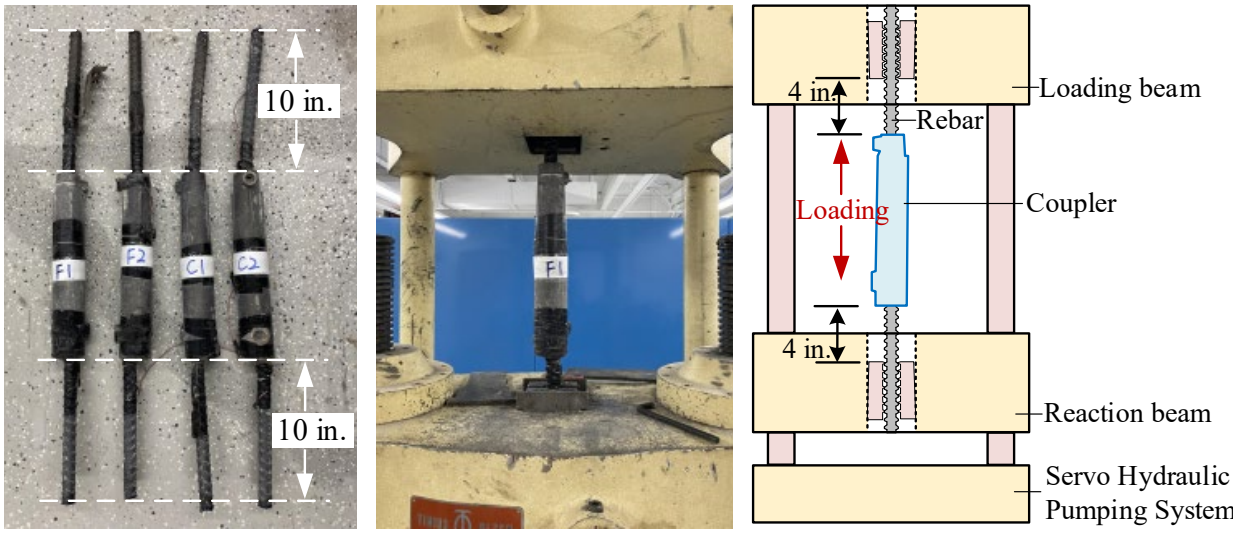


(a) Specimens (b) Test setup (c) Schematic setup

**Figure 3.10** Pull out test configuration

# 4. STATIC TEST RESULTS AND DISCUSSIONS

In order to understand the load distribution among the various components (i.e., rebar, coupler, grout, and concrete) within the GSS region and evaluate the overall performance between the column base connector and the footing top connector, the measured strain of both the rebar and coupler are summarized and compared. These strains are converted into load distributions based on relative stiffness, and the resulting experimental load distributions are compared to theoretical predictions. With a foundational understanding of the materials' load-bearing characteristics under compressive and shear loads, it is important to know and understand how forces travel from one element to another, which is crucial for evaluating structural integrity and safety.

## 4.1 Response for Axial Compression Loading Stage

The strain data from both the reinforcement and the grouted sleeves are represented by the solid lines in Figure 4.1. To simplify the structural response for the load increase phase and to capture the mean value of strain for static loading phase, the solid curves are approximated using a bilinear fitting, shown as the dashed lines in Figure 4.1.

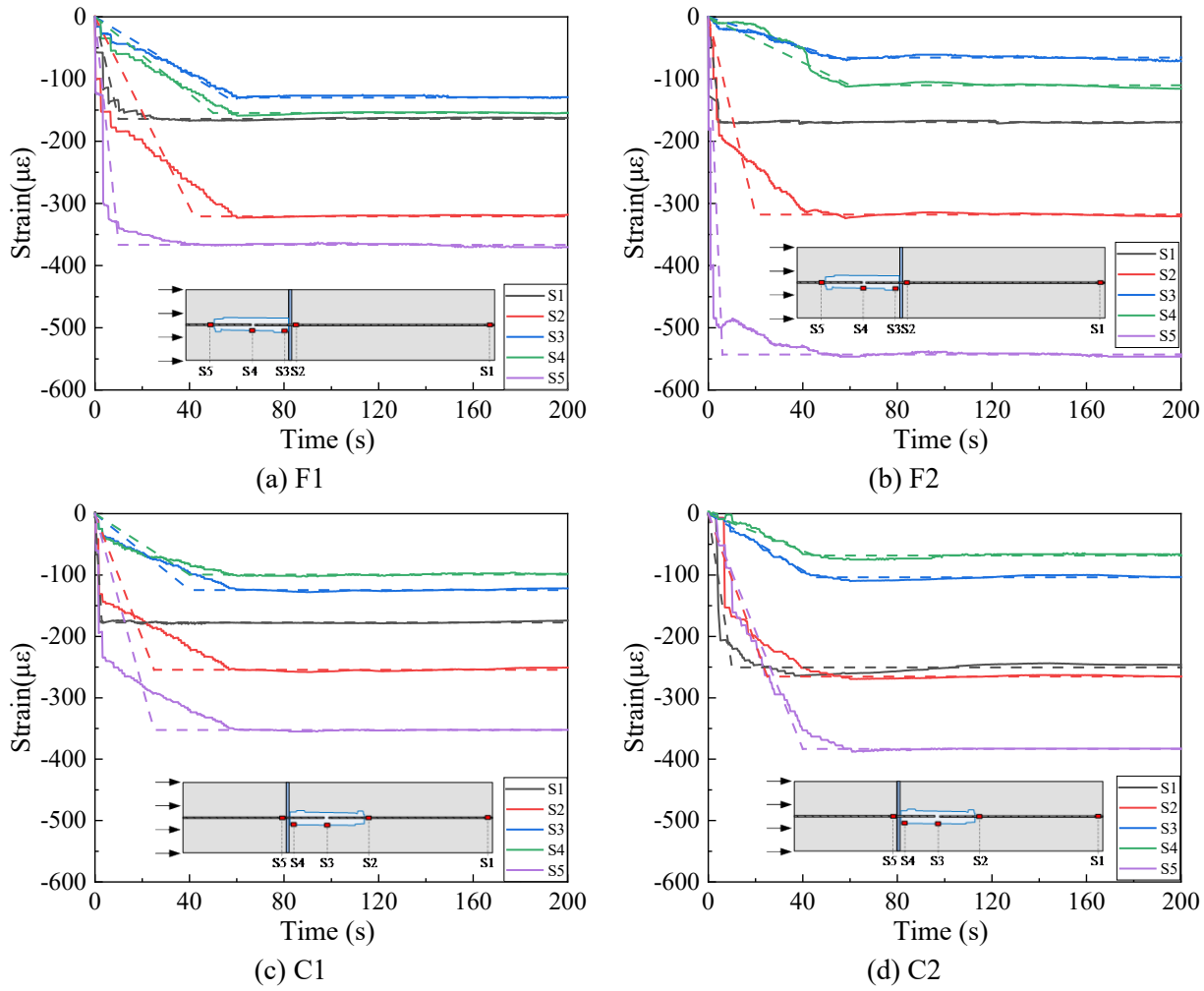


**Figure 4.1** Strain-time history (solid lines: test data; dashed lines: bilinear fitting)

In Figure 4.1, all curves exhibit a similar trend; starting from a value of 0, they peak at a negative maximum, and then stabilize at a specific value for the remainder of the observation period. However, the time taken to reach this peak value varies based on the different strain gauge locations. For specimens F1 and F2, sensors S2, S3, and S4, which are located inside the cylinder, show the same behavior as the applied load: they increase at a steady rate up to $t = 60$ seconds before plateauing. On the other hand, strain gauges S1 and S5, positioned close to the sides, record more rapid increase rates compared with the others. Due to the specimens' side-surface imperfections, the applied compressive load cannot distribute uniformly across the side sections. As such, it causes stress concentrations at both sides so the strain gauges near these areas show rapid changes in strain. As stress waves propagate through the material, this localized effect reduces from the sides to the middle. This explains why the interior gauges record the same steady rate as the applied load. Specimens C1 and C2 follow this pattern as well, as evidenced by the faster initial rising rate observed in gauge S1.

When analyzing with the ultimate strain values in Figure 4.1, several findings are highlighted: (1) The rebar strain from sensors S1, S2, and S5 are consistently higher than the strain on the GSS recorded by gauges S3 and S4. It is well known that the load distribution in a structure is largely governed by the stiffness of its components, defined as the product of its modulus of elasticity ($E$) and cross-sectional area ($A$). GSS has a higher stiffness relative to the rebar, leading to less deformation of the GSS under the same load. (2) On the rebars, larger strains are observed closer to the load applied side; the recorded strains are highest at strain gauge S5, followed by S2 and then S1. When a compressive load is applied, due to the rough loading surfaces of the specimens, the load concentrates around the rebar. As a result, the rebar closest to the applied load must share a larger load than theoretically expected, leading to higher strains. As the load distributes through the structure, the concrete portion effectively takes more of the compressive load, resulting in less load and subsequently less strain on the rebars in the location farther away from the loading side. (3) On the GSSs, the strains measured in the middle of the sleeves are always higher than those at the sides. It can be observed that strains from S4 exceed the data from S3 in GSS-F specimens, while strains from S3 are larger than those obtained by S4 in GSS-C. This is caused by the bucket effect: when a cylindrical GSS is subjected to axial compression, the central portion of the sleeve tends to expand laterally, leading to larger deformations and higher strains in the middle compared with the sides.

To further understand the differential behavior between two types of connections, the average curves of fitting lines for each strain gauge from each category are compared in Figure 4.2. The data from strain gauge S1 are particularly valuable for comparison since they are located in the same position for both test setups. Compared with the shorter footing part, the column part plays a more significant role in the load transfer procedure. As the columns of GSS-C with the embedded couplers become stiffer, strain gauge S1 in GSS-C takes more compressive load than that in GSS-F. Additionally, for other strains on the rebars, larger strains, which are closer to the load applied side, are observed from the sensor in GSS-F. This observation further proves the second finding (2) discussed in the previous paragraph.

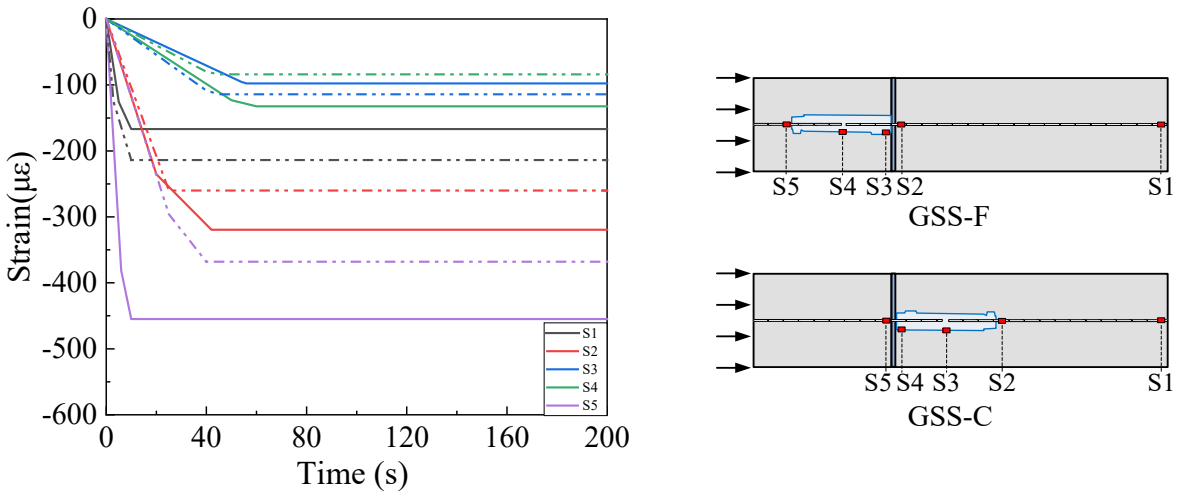


**Figure 4.2** Average curves for GSS-F and GSS-C (solid lines: GSS-F; dash-dot-dot lines: GSS-C)

## 4.2 Load Distribution Conditions

To further understand the load distribution, five cross-sections at the strain gauge locations are selected for analysis, as shown in Figure 4.3. Sections 1, 2, and 5 are comprised of rebar and concrete, while sections 3 and 4 include rebar, grout, GSS, and concrete.

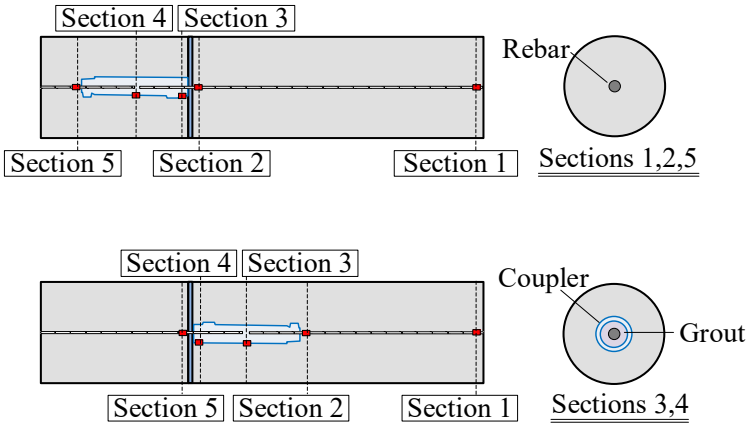


**Figure 4.3** Diagrams of sections

When the structure is in the ideal elastic condition, several typical assumptions are made: (1) the specimen is still under elastic limit, (2) the material has uniform properties at every point, (3) stress is uniformly distributed across the section, and (4) all materials are perfectly bonded with each other. These assumptions, except for the first one, are hard to achieve in the experimental test. Therefore, two methods of load distribution calculations are introduced for the ideal and actual conditions, respectively. In an ideal scenario, the basic load sharing principle is as follows: all materials deform together (i.e., plane sections remain plane), meaning they have the same strain across each section. According to the deformation formula for axial compression, the compressive load carried by each material is found by multiplying this strain by the product of its stiffness. Based on the strain compatibility, the load-carrying percentage of each material is determined by the relative proportion of its stiffness to the total stiffness as per the following equations:

$$P_{\mathrm{i}} = \varepsilon \cdot E_{\mathrm{i}} \cdot A_{\mathrm{i}} \quad \text{Eq. 2}$$

$$\text{Percentage} = E_{\mathrm{i}} \cdot A_{\mathrm{i}} / \sum E_{\mathrm{i}} \cdot A_{\mathrm{i}} \quad \text{Eq. 3}$$

Where: $P_{\mathrm{i}}$ is the load carried by each material, i = r, c, cp, and g, which represents the rebar, concrete, GSS, and grout, respectively. The modulus of elasticity of rebar and GSS is obtained from Table 3.2.

Under an actual condition, the load distribution is mainly calculated using the measured mean strain values of constant stages from Figure 4.2. For sections 1, 2, and 5, the loads carried by rebars are based on the measured strain, with concrete accounting for the remaining load, as shown in Eqs. 4 and 5. For sections 3 and 4, the actual strains in the coupler are derived from tests. The other three components bear the residual load. The load distribution percentages are also calculated by their relative stiffness to overall stiffness, as shown in Eqs. 6 and 7. Graphical representations of the material load-bearing percentages can be found in Figure 4.4.

$$P_{\mathrm{r}} = \varepsilon_{\mathrm{r}} \cdot E_{\mathrm{r}} \cdot A_{\mathrm{r}} \quad \text{Eq. 4}$$

$$P_{\mathrm{c}} = \text{Total load} - P_{\mathrm{c}} \quad \text{Eq. 5}$$

$$P_{\mathrm{cp}} = \varepsilon_{\mathrm{cp}} \cdot E_{\mathrm{cp}} \cdot A_{\mathrm{cp}} \quad \text{Eq. 6}$$

$$P_{\mathrm{i}} = \left(E_{\mathrm{i}} \cdot A_{\mathrm{i}} / \sum E_{\mathrm{i}} \cdot A_{\mathrm{i}}\right) \cdot (\text{Total load} - P_{\mathrm{cp}}) \quad \text{Eq. 7}$$


**Figure 4.4** Load carried percentages

In the theoretical load distribution illustrated in Figure 4.4 (a), for regions without a grouted splice sleeve (non-GSS), concrete takes the majority of the compressive load (91%), while the rebars carry the remaining 9%. Therefore, concrete plays a critical role and should not be neglected in the static behaviors study of the GSS system. Along the loading direction, the amount of rebar load entering the sleeve at section 5 should be equivalent to this load exiting the sleeve at section 2. During the load transfer from the non-GSS region (at section 5) to the GSS region (at section 4), the rebar retains 8% of the load from itself, while the GSS and grout receive 21% and 2% of the load, respectively. The grout takes a smaller portion of the load than is expected to ensure the connection between the rebar and the sleeve.

In the experimental load distribution shown in Figure 4.4 (b) and (c), all the rebar loads exceed their respective theoretical values. This is because the coupler system is stiffer than the surrounding concrete, causing an increased concentration of load in the rebar area. As a component of the composite section, rebar can take more load compared with when considering it in isolation; especially on both ends of the coupler, the rebars are observed to carry 11% to 26% more load than the theoretical values predict. Particularly, loads concentrate at the end of the GSS connectors located at the column-footing interface, which may cause the rebar to fracture under extreme load. When comparing the inputting rebar load at section 5 to the outputting rebar loads at section 2, there is a reduction of 8% in GSS-C and 11% in GSS-F. The reason for load reduction during the load spreading is load absorption by the concrete. Regarding the load carried percentages in sections 3 and 4, distributions are similar with the idealized scenarios; the rebar maintains 7% to 8% of the load, while the grout carried 2% to 3%.

## 4.3 Response for Multi-step Lateral Ramp Loading Stage

The strain data from the specimens are shown by the solid lines in Figure 4.5. To reduce the effect of noise in the data and to better understand the underlying trends in strain development, the solid curves during the increasing loading phase are fitted by linear function, while the curves for the stable loading phase are represented by horizontal lines indicating the mean value, shown as the dashed lines in Figure 4.5. To compare the differential behavior of two connection types under the flexure condition, the average fitting curves for each strain gauge are represented in Figure 4.6.

All the specimens remain within their elastic region, and the resulting strain curve trends approximately follow the applied loading trends. In all curves, the data from sensors S1 and S2 show larger values than the data from sensors S3, S4, and S5. One reason for this is that the GSS exhibits higher stiffness related to the rebar, leading to less strain on the GSS. Another contributing factor is the restrictions on the footing parts, as the gauges located in the footing part capture less deformation than those in the column part. Furthermore, the strain from gauge S3 is greater than that recorded by gauge S4 because the point load location results in a larger moment at the gauge S3 location.

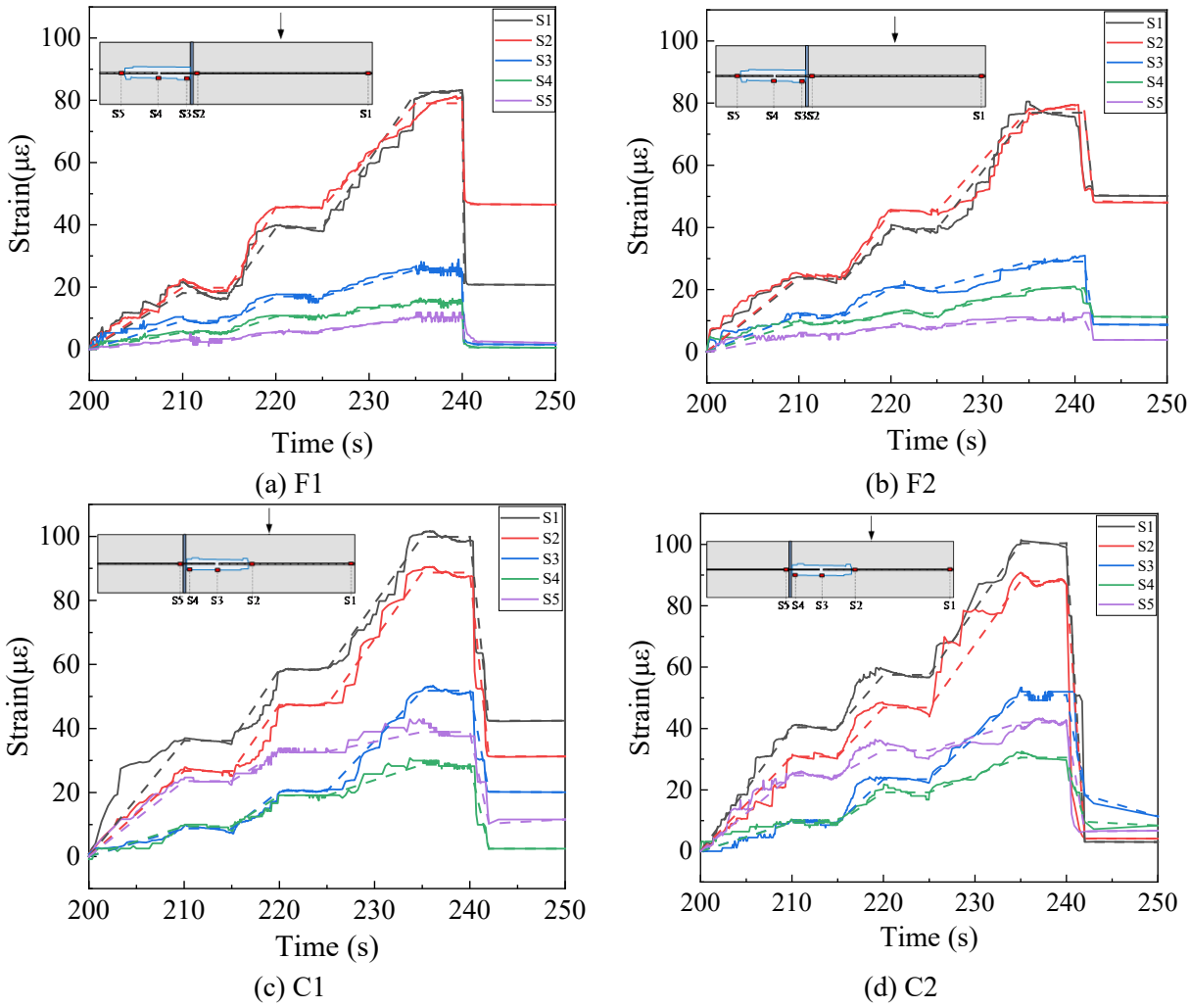


**Figure 4.5** Strain-time history (solid lines: test data; dash lines: bilinear fitting)

In Figure 4.6, all strain curves from specimens GSS-C lie above those from GSS-F. For the data comparison, strain gauge S1 in GSS-C exhibits a greater flexure strain compared with that in GSS-F. This is caused by more stiffness provided by the embedded couplers in GSS-C's column, leading to higher stress concentrations in the column base, and potentially diminishing the lateral load capacity on the column base connector. Importantly, this phenomenon is not isolated to static shear loading alone but extends to other lateral dynamic loads, such as earthquakes and vehicle impacts. Pantelides et al. report that the structures with GSSs in footings exhibit a more ductile response and better energy dissipation capacity compared with specimens with couplers in columns [40], [48]. Our study contributes valuable data support and experimental insights to further understand and support their conclusion. As for strain gauges S2 to S5, these sensors detect higher strains due to a larger portion of moments that is distributed in the GSS-C's coupler region.

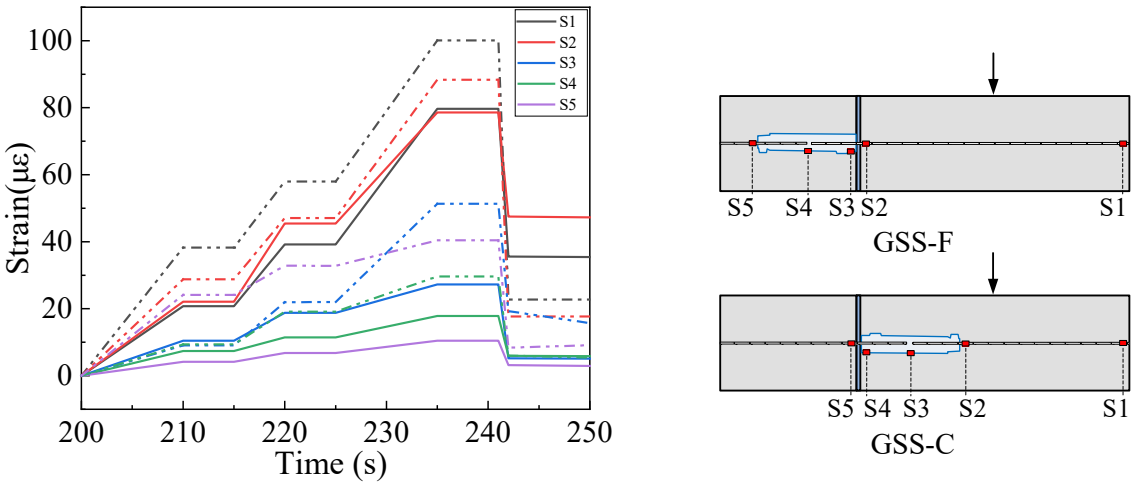


**Figure 4.6** Average curves for GSS-F and GSS-C (solid lines: GSS-F; dash-dot-dot lines: GSS-C)

## 4.4 Mechanics of compressive load transfer

During the application of incremental compressive force on the bottom side of the specimens, three main load paths of the cylinder with GSS operate as follows: (1) Concrete -> rebars: the compressive stress is initially generated in the concrete. Subsequently, this stress is transferred to the reinforced bars mainly through the mechanical interlock action of the ribs on these rebars. (2) Concrete -> GSS -> grout -> rebars: the compressive stress from the concrete is also transmitted to the pre-embedded GSS due to the extrusion action on both sides of the sleeve. The complex confinement actions are then generated within the sleeve; these processes are explained in detail in subsequent sections. Ultimately, the stress is carried by the infilled grout then passed to the rebars. (3) Concrete -> grout -> rebars: a portion of the compressive stress is directly transferred to the infilled grout. This contributes to the confining effect within the GSS, after which the stress is relayed by the rebars. The above main load paths are shown in Figure 4.7 (a).

Given the complicated internal characteristics of GSS, the sleeve can be divided into four segments: ridged, non-ridged, tapered, and tapered-ridged. In the ridged segment, the sleeve applies the confinement forces on the grout. These can be resolved into normal and longitudinal forces, which are perpendicular and parallel to the grouted sleeve axis, respectively, as shown in Figure 4.7 (b) (d). The normal componential stress provides radial confinement on the grout to restrain the volumetric expansion of grout. Concurrently, the longitudinal componential stress helps with longitudinal confinement and further prevents the slippage of the grout and horizontal movement of the rebars. Moreover, the longitudinal componential forces are caused by the interlocking mechanics. While chemical adhesion and friction also contribute to the force in the longitudinal direction, their contributions are typically too small to be considered significant. With regard to the non-ridged segment, the confinement force on the grout can also be decomposed into normal and longitudinal components. Specifically, the normal componential stress mainly stems from two factors: the radial confinement stress caused by Poisson's effect when the sleeve contracts along the axial direction, and the confinement stress caused by the expansion of grout along the radial direction. However, the longitudinal componential stress is dependent on chemical adhesion and friction between sleeve and grout. For the tapered segment and the tapered-ridged segment, the transfer mechanisms of normal componential forces are the same as that of the non-ridged segment and the ridged segment. However, due to the inclined internal surface of the sleeve, these tapered segments provide more effective longitudinal componential stress than those non-tapered segments, thereby enhancing the bond strength between the sleeve and the grout.

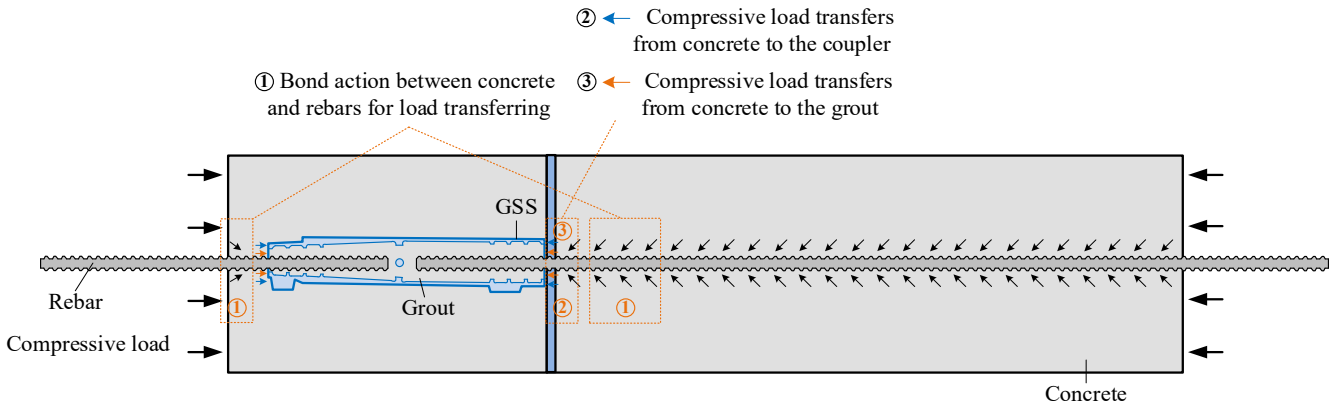


(a) Mechanism diagram of load transfer within the specimen

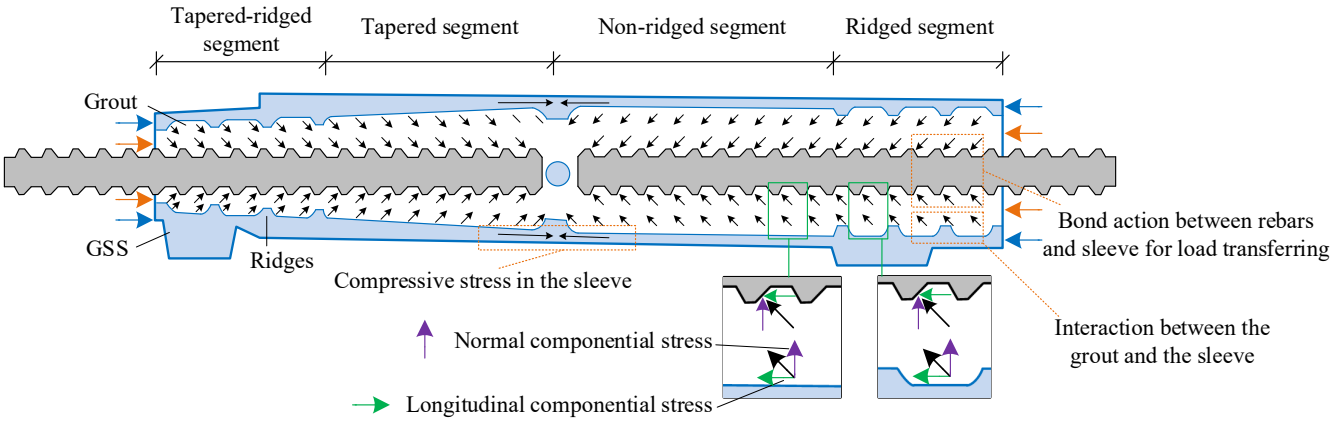


(b) Mechanism diagram of load transfer within the GSS system

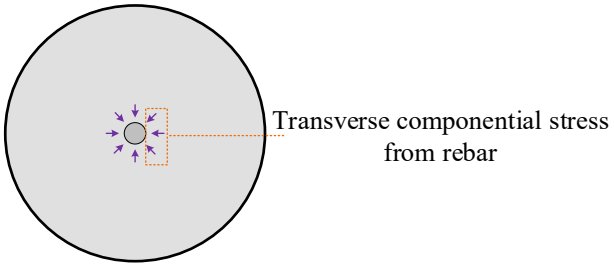


(c) Distribution of confinement stress in the concrete

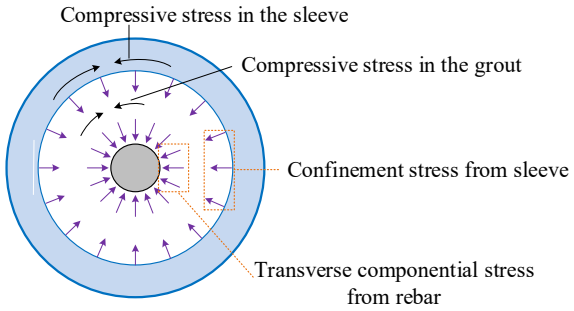


(d) Distribution of confinement stress in the sleeves

**Figure 4.7** Mechanics of compressive load transfer

## 4.5 Mechanics of Lateral Load Transfer

Based on the principles of load distribution mechanics under compressive loading described earlier, the lateral load transfer behavior is introduced in this section. When a lateral load is applied, both bending moment and shear forces are generated in the specimens, as shown in Figure 4.8 (a). The materials located above the neutral axis are under compressive stress while those below the neutral axis are subjected to tensile stress. The distribution of shear stresses significantly changes at the supports and the point of load. The flexural and shear stresses are efficiently transmitted from concrete to the rebar, primarily through the mechanical interlock action of the ribs on the rebar. Within the embedded GSS system, these stresses are also transferred to GSS and the grout components. Tensile stresses are particularly concerning as they most likely lead to connection failures between the rebar, grout, and GSS. As incremental lateral force is applied to the cylinder, cracks begin to develop in the grout once it reaches the cracking tensile strength. These cracks can be classified as either transverse cracks or splitting cracks based on their orientation.

To control the grout cracking, confinement forces are provided by the sleeve; these forces are generated mainly by the mechanical interlock in the ridged segment and produced by the wedge action of steel bars and the chemical adhesion and friction between the sleeve and the grout in the non-ridged segment. The confinement forces can also be decomposed into normal and longitudinal components, as shown in Figure 4.8 (b) (d). The normal componential stress provides radial confinement on the grout to delay the propagation of the splitting cracks along the radial direction. Meanwhile, the longitudinal componential stress helps resist the development of transverse cracks, thereby preventing slippage of the grout and the rebars.

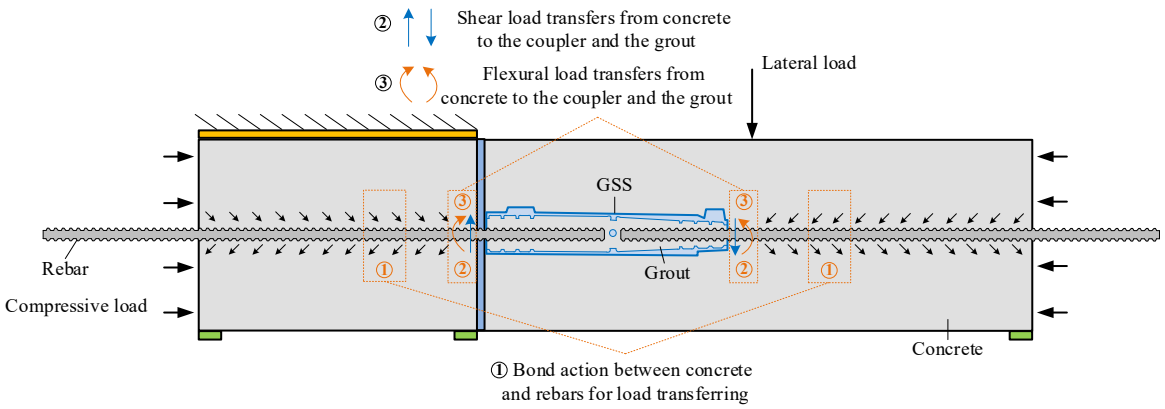


(a) Mechanism diagram of load transfer within the specimen

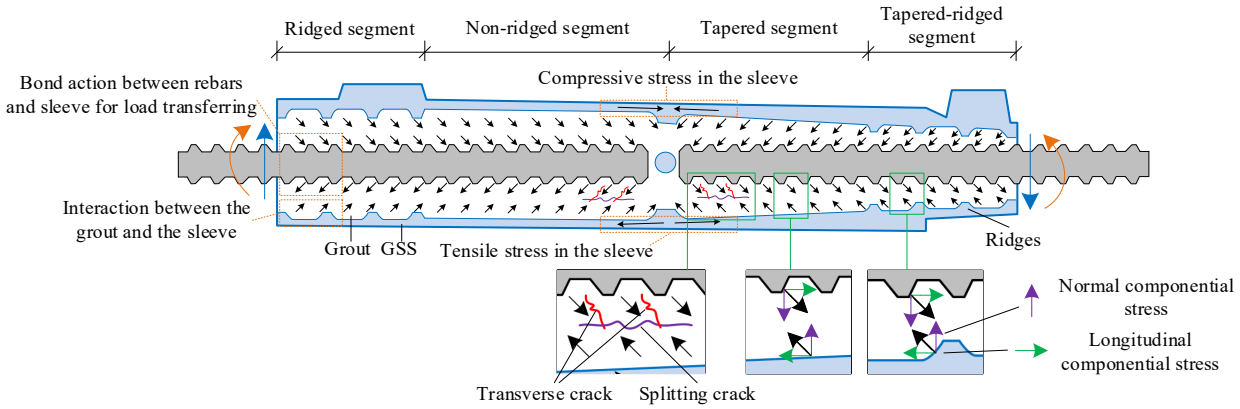


(b) Mechanism diagram of load transfer within GSS system

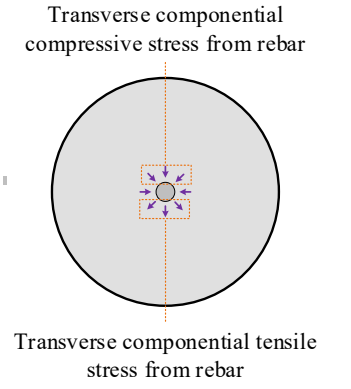


(c) Distribution of confinement stress in the concrete

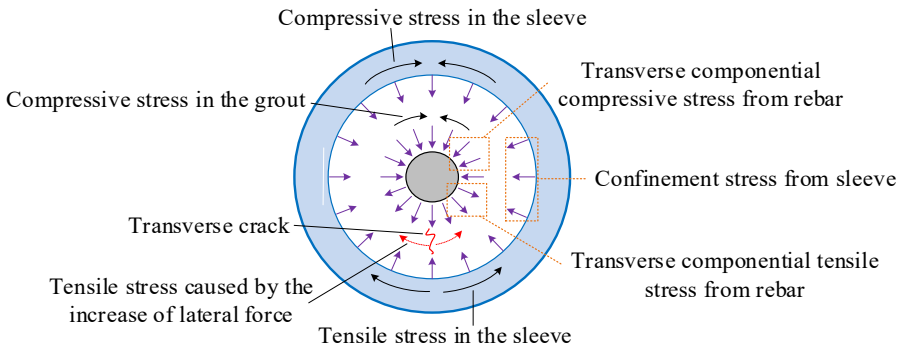


(d) Distribution of confinement stress in the sleeves

**Figure 4.8** Mechanics of lateral load transfer

# 5. DYNAMIC AND PULL-OUT TEST RESULTS AND DISCUSSIONS

## 5.1 Dynamic Response and Failure Modes

In order to evaluate the lateral impact resistance of PC columns with GSS connectors, four crucial aspects of evaluation are conducted: impact force-time relationships, strain-time relationships, failure processes, and local damages on the interface section. The dynamic response and failure modes of precast columns with GSS connectors can attain a comprehensive understanding of their impact resistance capacities.

### 5.1.1 Impact Force-time Relationships

Figure 5.1 presents the impact force-time relationships of the test specimens. All curves are comprised of three similar stages: first peak impact stage (I), second peak impact stage (II), and unloading stage (III). In the first peak impact stage, the sudden impact load applied by the actuator head causes severe vibration of the specimens, represented as the first significant fluctuation. As the first contact between the actuator and the specimen occurs, the impact force sharply increases from zero to its first peak value and suddenly decreases to a lower level; it then fluctuates around a constant value until the beginning of second peak impact stage. In the second stage, the actuator maintains contact with the specimen. Due to the increasing applied displacement, the contact load rises to the second peak value. After reaching the second peak, the actuator starts to return from the maximum displacement back to the initial location, leading to the reduction of impact load. In the unloading stage, the contact load instantly drops to zero as the contact area between the actuator and the specimen reduces to zero.

Table 5.1 compares four critical test results for specimens: first peak force, duration of first peak stage, second peak force, and duration of second peak stage. The first peak forces of specimens F1, C1, F2, and C2 are 47.02, 54.84, 55.85, and 61.84 kips, respectively. Notably, within the same impact velocity, specimen C1's first peak force is 17% higher than F1's, and C2's first peak force exceeds F2's by 11%. Similarly, this trend is observed in the second peak stage, where C1's second peak force is 52% higher than F1's, and C2's is 35% higher than F2's. This phenomenon is attributed to more stiffness provided by the embedded couplers in GSS-C's column, leading to higher load concentrations in the column and potentially diminishing lateral anti-impact capacity of the column base connector. Regarding the tests on the same category of connection, the first peak force of F2 is 19% larger than that of F1; similarly, the first peak force of C2 is 13% larger than that of C1. This same phenomenon is found in the second stage as well. The increased impact peak loads are caused primarily by the higher impact velocity in the second test group, which suggests that the structures exhibit more vulnerability under a high-velocity impact.

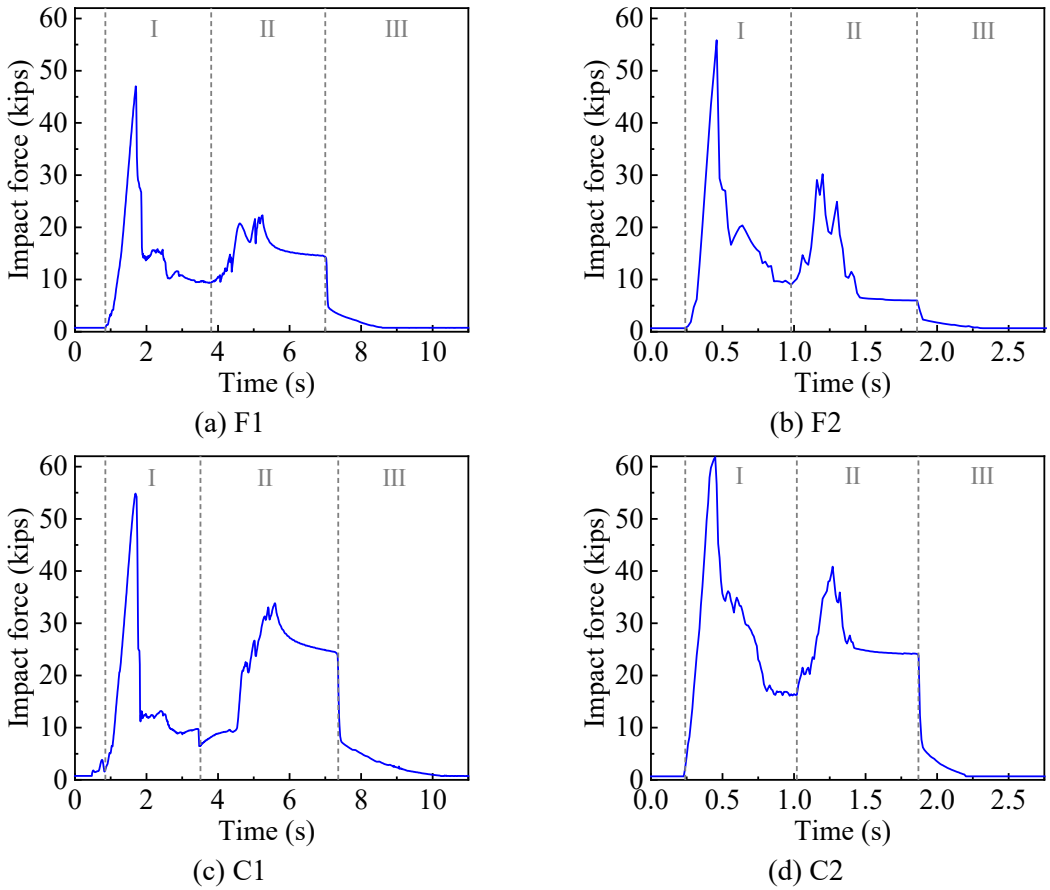


**Figure 5.1** Impact force-time relationships

A comparison between the peak forces of the first and second stages reveals that the first peak force always exceeds the second peak value. This is explained by the initial generation of cracks during the first stage, leading to the deduction of lateral stiffness of column. In addition, the longer duration happens in the second peak stage, compared with the first peak stage.

**Table 5.1** Comparison of impact force-time relationships

| Specimens | First peak force (kips) | Duration of first peak stage (second) | Second peak force (kips) | Duration of second peak stage (second) |
|---|---|---|---|---|
| F1 | 47.02 | 2.96 | 22.31 | 3.19 |
| C1 | 54.84 (+17%) | 2.66 (-10%) | 33.82 (+52%) | 3.85 (+21%) |
| F2 | 55.85 (+19%) | 0.74 | 30.18 (+35%) | 0.88 |
| C2 | 61.84 (+11%) (+13%) | 0.78 (+5%) | 40.84 (+35%) (+21%) | 0.85 (-3%) |

**Notes:** 1. The percentage values in black brackets indicate the differences between the two types of connections with same impact velocity. 2. The percentage values in orange brackets indicate the differences between the same type of connection with different impact velocities. 3. Example: for the first peak force of C1, 17%= (54.84-47.02) / 47.02*100%.

### 5.1.2 Strain of Rebars and Coupler-time Relationships

Figure 5.2 shows the strain-time relationships for the couplers and rebars measured during impact on the four specimens. For sensor S2 on specimen C2, strain data are collected up to 0.6 s, then the strain gauge is likely destroyed and ceases to record data due to significant damage at its mid-span location. When comparing impacts at velocities of 0.5 in./second (F1 and C1) versus 2 in./second (F2 and C2), the lower-velocity impact tests present strain fluctuation during the entire impact period, but only the response for first peak impact can be captured in tests F2 and C2. This is attributed to the limited sampling rate of five readings/second (5HZ).

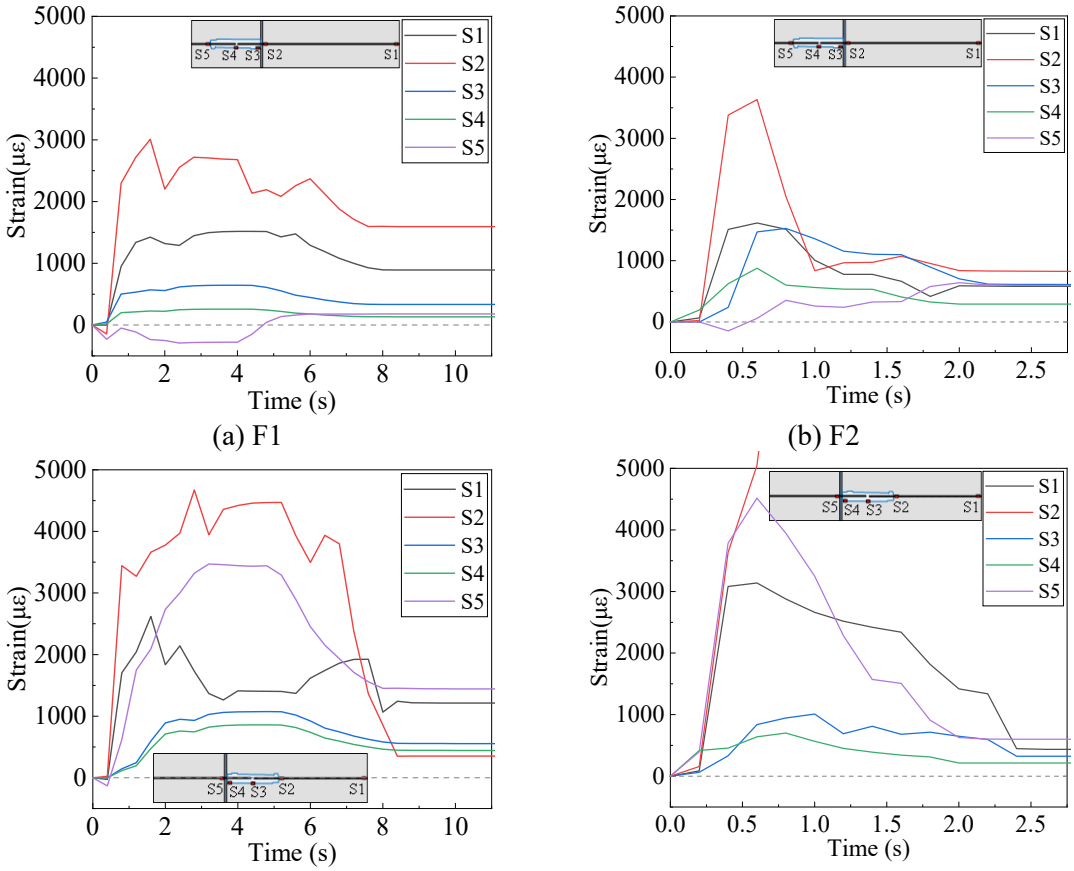


**Figure 5.2** Strain-time relationships for the couplers and rebars measured during impact

The first peak strain values observed by sensors S1, S2, and S5 on the rebar are summarized in Table 5.2. The larger deformations on rebar are attributed to the smaller relative stiffness of rebar, which is defined as the product of its modulus of elasticity and cross-sectional area, leading to more strain on rebars. Sensor S5 on specimens GSS-F, located in the footing part, captures less fluctuation during testing because of the serious restraint on the footing section. The comparison of the peak strains in Table 5.2 reveals two trends. (1) Due to the stiffer column with the embedded coupler, specimens GSS-C consistently demonstrate higher flexural strain than those in specimens GSS-F. This indicates that structures with GSSs in the footings exhibit a more ductile response and better impact resistance compared with specimens with couplers located in column sections. (2) Specimens subjected to higher velocity impacts and greater impact loads experience more deformation. This is an expected outcome, and the physical testing in this experiment reflects this.

**Table 5.2** Comparison of first peak strains (unit: με)

| Specimens | S1 | S2 | S5 |
|---|---|---|---|
| F1 | 1,517.9 | 3,008.4 | -291.2 |
| C1 | 2,619.2 | 4,673 | 3,470.4 |
| F2 | 1,616.4 | 3,633.8 | 352.5 |
| C2 | 3,139.2 | 5,048 | 4,514.9 |

### 5.1.3 Failure Processes

Figure 5.3 illustrates the failure processes of the specimens at four characteristic moments: (I) when the actuator head initially contacts the column, several small flexural cracks generate at the mid-span of the column part; (II) as the impact load reaches its first peak value, the new cracks form and develop significantly; (III) as the lateral displacement increases to the maximum position, crack width expands continuously without the development of any new cracks; (IV) after impact, the specimens ultimately show complete failure.

The overall failure processes of specimens F1, F2, and C1 are generally consistent. All major damage occurs away from the GSS region, indicating that the coupler connections remain bonded during the impact and the load is transferred through the coupler connection. For specimens F1 and C1, after the appearance of flexural cracks, diagonal shear cracks propagate from the impact location to the edge of the right support under the column. Shear cracks then expanded rapidly with the increasing displacement. Finally, the concrete shear fractures are the main cause of structural failure rather than the initial flexural cracks. This is because the combined effect of axial compression force and impact load leads to high shear stress at the right part of column. In addition, the lack of stirrups in the specimen results in inadequate resistance against shear forces. For specimen F2, both flexural cracks and shear cracks develop and contribute to the final failure.

As illustrated in Figure 5.3 (d), specimen C2 develops a unique failure pattern with a vertical crack at the column's mid-span, which propagates through the entirety of the cross section until specimen failure. This is because the coupler's right end is located on the middle point of the column part where higher stress concentrates during the higher velocity impact. Major cracks may occur within the grout, leading to the loss of bonding on the right narrow end of the coupler. Once this bond failure occurs, the mid-region's flexural capacity reduces rapidly, leading to the main flexural fracture. It also indicates that the GSS-C specimens may offer less impact resistance compared with GSS-F specimens under higher velocity impacts.

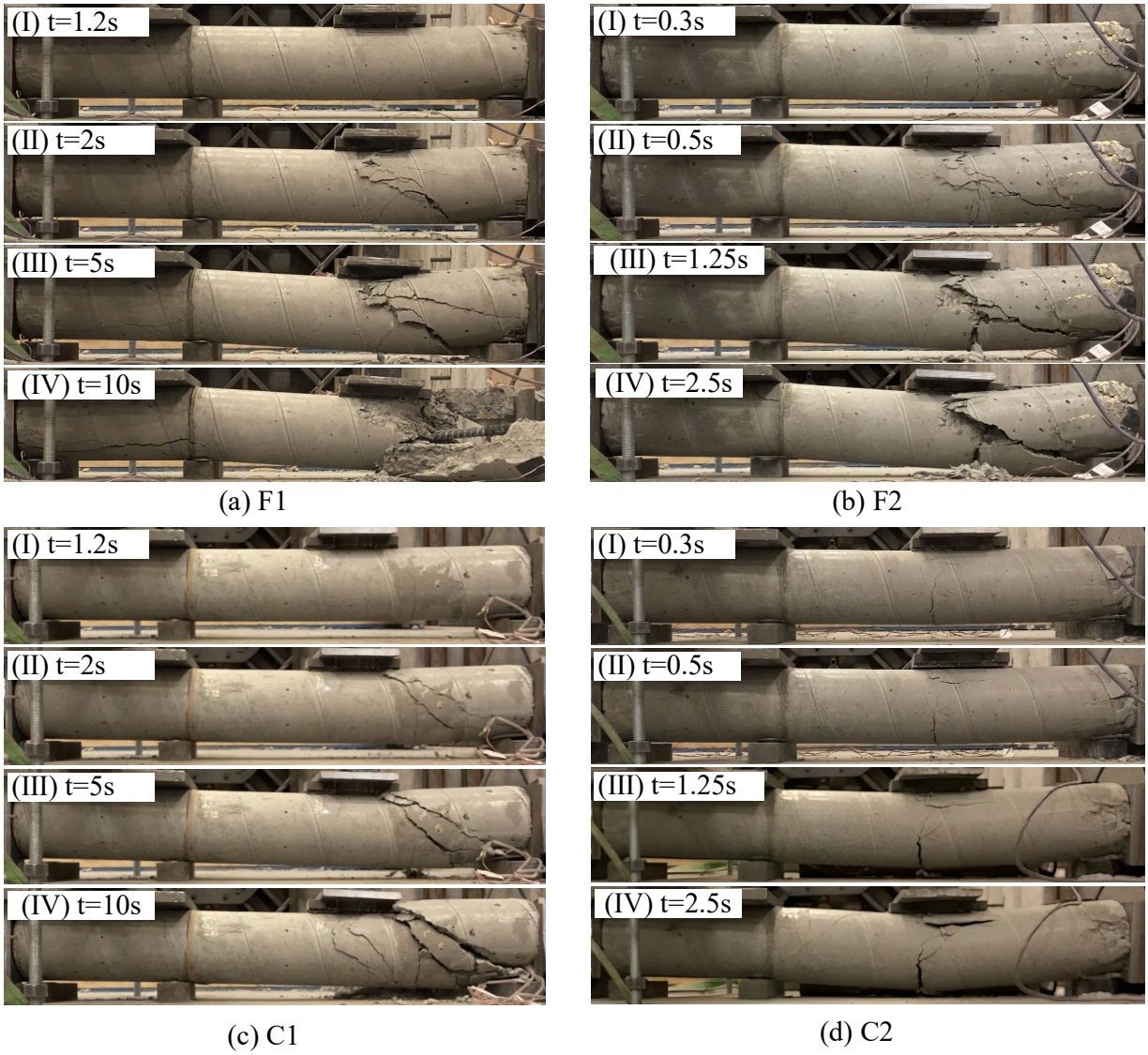


**Figure 5.3** Failure processes of specimens: (a) F1, (b) F2, (c) C1, and (d) C2

### 5.1.4 Local Damage at Interface

To further understand the damage on potential vulnerable areas, Figure 5.4 details the localized damage at the interface between the column and footing parts, where all major wide cracks are observed on the left side of the grout bed. In addition, the other horizontal cracks occur around the bottom support and top fixed plate from the top views. Notably, compared with specimens C1 and C2 (GSS-C), specimens F1 and F2 (GSS-F) exhibit more severe damage with crack widths measuring 0.27 in. and 0.4 in., respectively. The two relatively narrow cracks are shown in specimens C1 and C2 with widths of 0.04 in. and 0.09 in., respectively, revealing a relatively intact concrete connection area. This also indicates that transition of the flexural and shear action from the column part to the footing part is successful in GSS-C because the GSS connectors are located in the column base. These preliminary observations provide valuable documentation, which can later be used for calibrating and refining numerical models to simulate the behavior of GSS connections under dynamic loads. The insights offer a foundation for future experimental and numerical analyses in the field, driving more predictive and accurate modeling of GSS connection performance under impact loads.

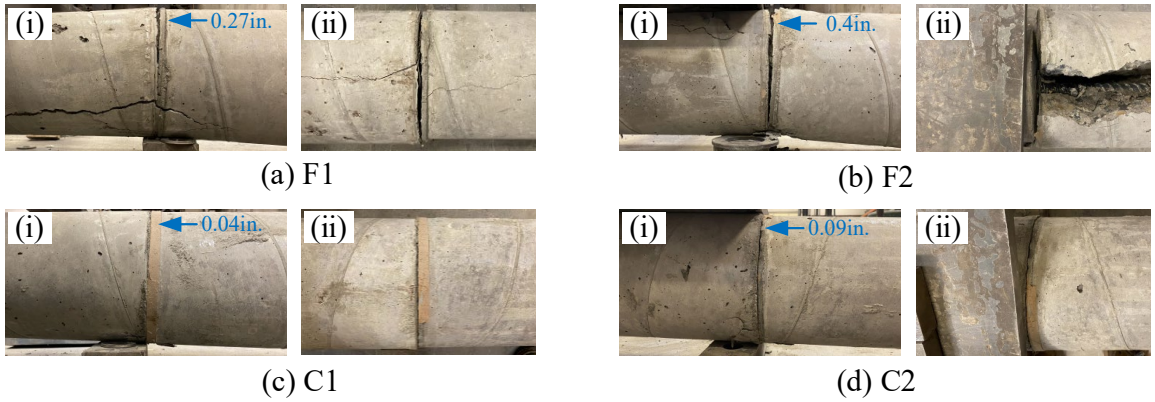


**Figure 5.4** Local damage at interface: (i) Front view; (ii) Top view

## 5.2 Pull-out Response and Failure Modes

To investigate the reduction of bond strength in post-impact GSS connectors, failure modes of post-impact couplers in two categories of GSS specimens are revealed. For further quantitative analysis, ultimate tensile stresses between post-impact and undamaged (healthy) couplers are compared to obtain a bond strength reduction percentage of damaged couplers after impact load.

### 5.2.1 Pull-out Failure Modes

Images of the specimens, post testing, are shown in Figure 5.5. There are two typical failure modes of the GSS specimens: (a) rebar tensile fracture failure, and (b) bond-slip failure. In general, the tensile capacity of the connection mainly depends on the tensile strength of the rebar and the bonding strength generated between the rebar and the grout material. For specimens F1 and F2 (GSS-F), tensile fracture failures of rebars are notably observed near the narrow open end of the sleeve. It indicates that the grout bonding strength inside the coupler is higher than the ultimate tensile strength of rebars. The intact grout surfaces at both ends of the coupler can also be observed after impact. While the other two specimens, C1 and C2 (GSS-C), exhibit a distinct failure mode, where the embedded bars pull out from the sleeve as a result of bond-slip failure. The one reason for bond-slip failure is the grout cracks at the narrow end of the coupler after impact, which diminishes the effective contact area between the spliced bar and grout, thereby reducing the mechanical bond capacity. The other reason is that axial elongation of yielding bars decreases their cross-sectional area, reducing the interlocking mechanics and friction which is essential for maintaining bond strength, ultimately affecting the tensile capacity of the connection system.

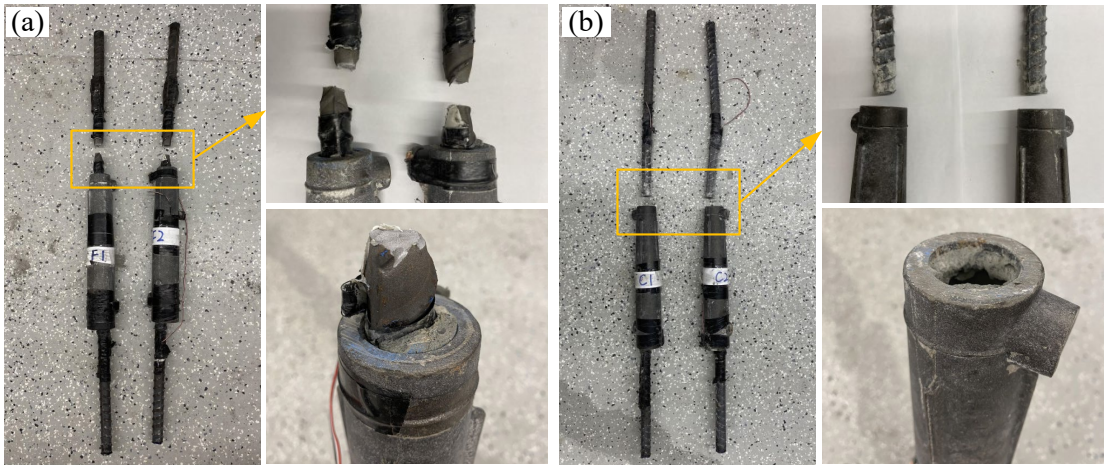


(a) rebar tensile fracture failure (b) bond-slip failure

**Figure 5.5** Failure modes of GSSs

### 5.2.2 Residual Tensile Capacity

To determine the residual tensile capacity of the GSS system under tensile loading, the four strain-stress curves of each specimen are plotted in Figure 5.6. Due to initial slack from two clip ends in the testing setup, the initial stress-strain relationships are nonlinear (referred to here as the "soft-start zone"). Normally, this zone is not considered as a portion of the stress-strain curve. However, to show the data of specimen C2, the portions of curves on the soft-start zone are kept.

Haber et al. tested three healthy (i.e., not impacted or damaged) GGS connector specimens bonding two No. 8 bars under static tensile load with pre-yield displacement rates of 0.01875 in/sec (1.125 in./min) [46]. The failure modes of this testing were bar ruptures away from the coupler region. The average yield and ultimate stresses were 66.2 ksi and 108.5 ksi, respectively (listed in Table 5.3).

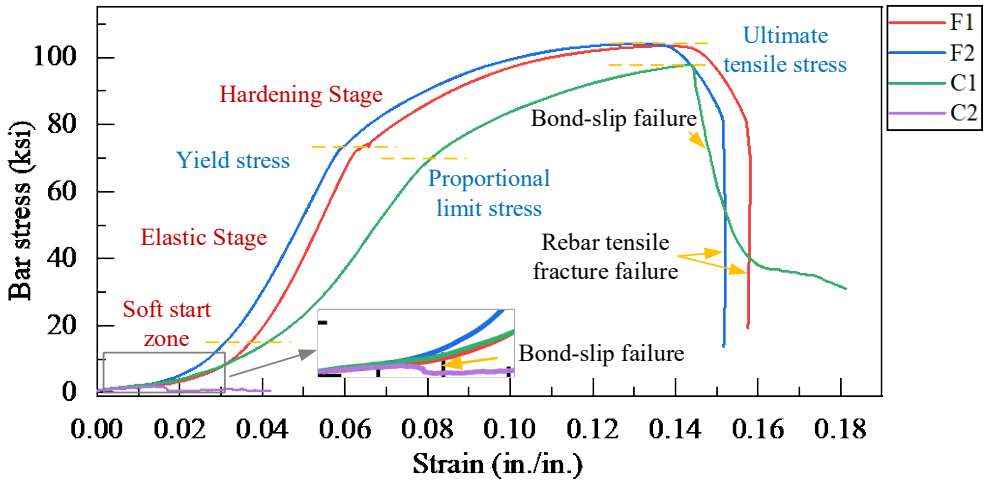


**Figure 5.6** Bar stress – strain curves

**Table 5.3** Comparison of stress-strain relationships

| Specimens | Yield stress/proportional limit stress (ksi) | Ultimate stress (ksi) |
|---|---|---|
| Haber [46] | 66.2 | 108.5 |
| F1 | 73.6 (+ 11%) | 103.1 (-5%) |
| F2 | 72.8 (+ 10%) | 103.7 (-4%) |
| C1 | 68.2 (+ 3%) | 97.8 (-10%) |
| C2 | - | 2.55 (-98%) |

**Notes:** The percentages values in brackets indicate the differences between the test results with the data from Haber's paper; for example, the yield stress of F1, 11% = (73.6-66.2) / 66.2*100%.

Beyond the initial nonlinear soft-start zone, specimens F1 and F2 exhibit similar behaviors to the healthy Haber specimens, including four typical stages: elastic, yielding, hardening, and ultimate tensile failure stages. During the initial elastic phase, both F1 and F2 demonstrate identical Young's modulus of elasticity, achieving yield stresses at 73.6 ksi and 72.8 ksi, respectively. These yield stresses are 10% to 11% higher than those observed for the healthy couplers. This is due to not being damaged and the higher loading rate applied in Haber's test. Subsequent to the yielding phase, both specimens exhibit good ductility responses and plastic deformations, ending with ultimate tensile strengths of 103.1 ksi and 103.7 ksi; only 4% to 5% below that of the healthy couplers. This indicates that post-impact couplers in GSS-F have minimal reduction of tensile capacity and maintain good bond performances. After reaching this peak, the curves decline, accompanied by rebar necking and eventual fracture with a loud noise. This is attributed to the bonding strength between the spliced bars and the grout material being higher than the rebar tensile strength.

Alternatively, the stress-strain profiles for specimens C1 and C2 are totally different. The initial elastic segment of C1's curve closely approximates a linear response characteristic of ductile materials, with a reduced modulus of elasticity. Moreover, no obvious yield point can be observed after elastic deformation. A proportional limit stress of 68.2 ksi can be identified as the end of the elastic stage, surpassing that of the healthy coupler by 3%. Following this phase, the materials no longer reflect Hooke's Law, attaining an ultimate strength of 97.8 ksi; 10% below the pre-impact coupler value and indicating a 10% loss in tensile strength due to impact. The curve then drops abruptly and the spliced bar at the narrow open end of the coupler is slowly pulled out without significant rebar necking or audible fracturing, typical of a brittle failure mode. This failure is primarily due to pre-fracture bonding failures between the splice bars and grout since the grout in the sleeve cannot restrain the movement of rebar. For specimen C2, the curve demonstrates little residual tensile capacity, with an ultimate tensile strength of merely 2.55 ksi; reflecting a 98% reduction from the healthy coupler followed by bar pull out from the coupler's narrow opening.

# 6. CONCLUSIONS

## 6.1 Static Study

In this study, two groups of PC specimens with GSS connectors at different locations are tested under sequential compressive and lateral loads to obtain strain-time history at five critical regions on rebars and GSSs. Based on the measured data, compressive and shear behaviors between two connector categories are discussed, and load distribution percentages of each component of the GSS system are then determined and compared with the theoretical predictions. Transfer mechanics of compressive and lateral loads through the precast system are revealed. The main conclusions of this study are the following:

(1) Because of the stiffer columns with the embedded couplers, column parts of pier base connections (GSS-C) exhibit greater compressive and flexural strains than those in footing top connections (GSS-F). In pier base connections, higher stress concentrations in the coupler joint are observed, which may diminish the lateral load capacity of precast structures. It can also be extended to lateral dynamic loads, indicating that structures with GSSs in footings exhibit a more ductile response and better energy dissipation capacity compared with specimens with couplers in column sections.

(2) In both theoretical and experimental load distribution, the grout takes the smallest portion (2% to 3%) of the load that is expected to ensure the connection between the rebar and the sleeve. Meanwhile, concrete not only takes most of the load across all critical sections but absorbs load during the load distribution through the GSS system. Therefore, concrete plays an indispensable role in the study of static behaviors of GSS system.

(3) In experimental observations, rebars on both open ends of coupler carry loads that are 11% to 26% greater than theoretical predictions. This indicates that loads concentrate at the ends of the GSS connectors. Such concentration at the column-footing interface may lead to potential rebar fracture under extreme load conditions.

(4) The load transfer mechanics in the cylinders with GSSs are revealed as three main load paths: concrete–rebars, concrete–GSS–grout–rebars, and concrete–grout–rebars. These pathways can help to understand how forces travel from one element to another during compressive and lateral loading, which is crucial for evaluating structural integrity and safety.

(5) When an increasing lateral force is applied to the cylinder, transverse cracks or splitting cracks begin to develop in the grout once it reaches the cracking strength. The confinement forces from GSSs are decomposed into normal and longitudinal components; normal componential stress acts to delay the propagation of the splitting crackswhile longitudinal one helps to resist the development of transverse cracks.

## 6.2 Dynamic and Post-damaged Study

In this study, four PC specimens with two types of pier-footing connections are tested under two different impact velocities to analyze and compare impact force-time relationships, strain-time history, crack propagation processes, and final overall and local damage of specimens. After that, pull-out tests are performed on the post-impacted GGS connectors to reveal the failure modes and bond strength reduction percentage of post-damage couplers. The main conclusions of this study are the following:

1) The impact force-time relationships of specimens can be divided into three stages: the first peak impact stage, the second peak impact stage, and the unloading stage. Under the same velocity impact, specimens with the coupler in the column (GSS-C) always exhibit larger first and second peak impact forces than specimens with the coupler in the footing (GSS-F). This phenomenon is attributed not only to the distance from the impact location to the coupler bust also to the stiffness provided by the embedded couplers in the GSS-Cs, leading to higher load concentrations in the column. On the other hand, for the same joint category, the first and second peak of impact forces increase with the higher impact velocity. This suggests that these connections exhibit more vulnerability under a high-velocity impact.

2) The failure of specimens F1, C1, and F2 similarly results from diagonal shear fractures, indicating that shear forces play a critical role in the structural failure of these specimens. In addition, all observed major damage occurs away from the GSS regions, implying that the GSS connections maintain their integrity and bonding performance under impact loading. Alternatively, only one flexural crack, located on the right end of the coupler, occurs in specimen C2 as the main reason for this unique failure, caused by the loss of bonding on the narrow end of the coupler. It also indicates that GSS-C specimens exhibit lower impact resistance than GSS-F specimens, especially under high-velocity impacts. The optimizing placement of GSS connections in footings can avoid the risk of failure under dynamic loads and enhance the overall safety and durability of PC systems.

3) Another potentially vulnerable area is at the interface between the column and footing connection where specimens GSS-F exhibit wider cracks than those in specimens GSS-C. It indicates specimens GSS-C perform a more effective transition of flexural and shear action from the column to the footing, which is attributed to the GSS connectors located in the column base. Although these preliminary findings can provide valuable documents for calibrating and refining numerical models to simulate the behavior of GSS connections under the impact loads, full-scale testing is still crucial for accurately determining failure modes and understanding the comprehensive behavior of GSS connections under real-world dynamic loads.

4) GSS specimen failure modes are significantly related to the connection categories. In specimens GSS-F, rebar tensile fracture is observed near the coupler, indicating that the grout bonding strength inside the coupler is higher than the ultimate tensile strength of rebars. Conversely, in GSS-C specimens, bond-slip failure occurs at the narrow ending. This failure is primarily due to grout cracking within the post-impact coupler, which reduces the grout bonding strength below the ultimate tensile strength of rebars.

5) In evaluating the post-impact tensile performance of GSS connections, a distinct contrast emerges between the coupler types within the GSS-F and GSS-C specimens. The analysis reveals that GSS-F couplers experience a minimal decline in ultimate tensile capacity, with reductions limited to 4% to 5% compared with undamaged couplers, indicating their effective bond integrity after impact tests. In contrast, post-impact couplers in specimens GSS-C are more susceptible to tensile strength reduction, with reductions of 10% and an alarming 98% relative to the performance of healthy couplers. Such significant losses highlight the vulnerability of GSS-C connections under impact loading conditions. The application of GSS-C should be carefully considered, particularly for pier-footing construction in areas with high vehicle impact risk; while GSS-F connection is a high-performance bonding solution for ensuring enhanced durability and reliability under dynamic loading scenarios.

# 7. REFERENCES


[1] G. Shrestha, “Seismic studies of superstructure and substructure connections for accelerated bridge construction,” University of Nevada, Reno, 2018.

[2] S. C. Redd, “Strength, durability, and application of grouted couplers for integral abutments in accelerated bridge construction projects,” Iowa State University, 2016.

[3] A. DeJong, “Innovations in integral abutment connection details for accelerated bridge construction,” Iowa State University, 2019.

[4] M. P. Culmo, B. Lord, M. Huie, and B. Beerman, *Accelerated Bridge Construction: Experience in Design, Fabrication and Erection of Prefabricated Bridge Elements and Systems: Final Manual*, United States, 2011.

[5] M. J. Ameli, “Seismic evaluation of grouted splice sleeve connections for bridge piers in accelerated bridge construction,” The University of Utah, 2016.

[6] Businesswire, “Sterling Awarded $122.7 Million Design-Build Project in Utah Featuring Accelerated Bridge Construction,” Sterling Construction Company, Inc. Accessed: Mar. 25, 2021. [Online]. Available: https://www.businesswire.com/news/home/20210325005067/en/Sterling-Awarded-122.7-Million-Design-Build-Project-in-Utah-Featuring-Accelerated-Bridge-Construction

[7] E. Greeneway, “Seismic performance of mechanically spliced precast bridge columns with new couplers,” South Dakota State University, 2021.

[8] M. Tazarv and M. S. Saiidi, “Seismic design of bridge columns incorporating mechanical bar splices in plastic hinge regions,” *Engineering Structures*, vol. 124, pp. 507–520, 2016, doi: 10.1016/j.engstruct.2016.06.041.

[9] ACI Committee 439, “Types of mechanical splices for reinforcing bars,” Farmington Hills, MI: American Concrete Institute, Report No. ACI 439.3R-07., 2007.

[10] F. Lin and P. Zhao, “Behavior of grouted sleeve splice for steel profile under tensile loadings,” *Materials*, vol. 13, no. 9, pp. 1–19, 2020, doi: 10.3390/MA13092037.

[11] E. Henin and G. Morcous, “Non-proprietary bar splice sleeve for precast concrete construction,” *Engineering Structures*, vol. 83, pp. 154–162, 2015, doi: 10.1016/j.engstruct.2014.10.045.

[12] L. L. Liu, J. Z. Xiao, and T. Ding, “Finite Element Simulation Verification and Failure Mechanism of Grouted Sleeve Connections Under Loading,” *Gongcheng Lixue/Engineering Mechanics*, vol. 39, no. 12, pp. 177–189, 2022, doi: 10.6052/j.issn.1000-4750.2021.07.0560.

[13] AASHTO, *AASHTO LRFD Bridge Design Specifications*. Washington, DC., 2020.

[14] USGS, “Long-term National Seismic Hazard Map.” [Online]. Available: https://www.usgs.gov/media/images/2018-long-term-national-seismic-hazard-map

[15] M. Tazarv and M. S. Saiidi, “Design and construction of bridge columns incorporating mechanical bar splices in plastic hinge zones,” University of Nevada, Reno. Center for Civil Engineering Earthquake Research., 2015.

[16] AASHTO, *AASHTO LRFD Bridge Design Specifications, 7th Ed.* Washington, DC., 2014.

[17] Caltrans, *Caltrans Seismic Design Criteria, Version 1.7.* California Department of Transportation, Sacramento, CA., 2013.

[18] M. Wu, X. Liu, H. Liu, and X. Du, “Seismic performance of precast short-leg shear wall using a grouting sleeve connection,” *Engineering Structures*, vol. 208, no. September 2019, p. 110338, 2020, doi: 10.1016/j.engstruct.2020.110338.

[19] A. Ebrahimpour, B. E. Earles, S. Maskey, M. Tangarife, and A. D. Sorensen, “Seismic performance of columns with grouted couplers in Idaho accelerated bridge construction applications,” 2016.

[20] D. H. Qiao, Y. Q. Xu, X. Zhang, J. B. Pang, K. Liu, and S. J. Wang, “Seismic behaviour and size effect of column base joints with inverted exposed grouted sleeves,” *Journal of Building Engineering*, vol. 51, no. February, p. 104333, 2022, doi: 10.1016/j.jobe.2022.104333.

[21] M. Yang, Y. Jia, and D. Liang, “Shaking Table Tests and Simulations of Grouting Sleeve Connecting Prefabricated Bridge Piers,” *Symmetry (Basel)*, vol. 14, no. 652, pp. 1–15, 2022.

[22] R. D. Barton, M. J. Ameli, and C. P. Pantelides, “Precast Concrete Bridge Column-Footing Connections with Recessed Grouted Splice Sleeve Connectors,” *ACI Structural Journal*, vol. 119, no. 1, pp. 215–226, 2022, doi: 10.14359/51734218.

[23] G. C. Lee, M. Tong, and W. P. Yen, “Design of highway bridges against extreme hazard events: Issues, principles and approaches,” MCEER, University at Buffalo, State University of New York, 2008. doi: 10.1108/dpm.2009.07318cae.009.

[24] A. K. Agrawal, X. Xu, and Z. Chen, “Bridge-vehicle impact assessment,” University Transportation Research Center, 2011.

[25] E. Gordon and L. L. P. Seely, “Truck Driver Killed in 18 Wheeler Accident on Dolphin Road Overpass on I-30 in Dallas,” *Truck Accident Lawyer News*. Accessed: Jun. 15, 2012. [Online]. Available: https://www.truckaccidentlaw.org/blog/6046/truck-driver-killed-in-18-wheeler-accident-on-i-30-in-dallas/

[26] W. Patton, “Driver seriously hurt in bridge crash that obliterated rig,” *CDL LIFE*. Accessed: Sep. 28, 2021. [Online]. Available: https://cdllife.com/2021/driver-seriously-hurt-in-bridge-crash-that-obliterated-rig/

[27] T. V. Do, T. M. Pham, and H. Hao, “Impact force profile and failure classification of reinforced concrete bridge columns against vehicle impact,” *Engineering Structures*, vol. 183, no. September 2018, pp. 443–458, 2019, doi: 10.1016/j.engstruct.2019.01.040.

[28] W. Wang, J. Chen, R. X. Zhou, and J. Zhong, “A simplified coupled model for predicting dynamic processes of vehicle impact on pier columns,” *Structures*, vol. 41, no. May, pp. 997–1013, 2022, doi: 10.1016/j.istruc.2022.05.045.

[29] O. I. Abdelkarim and M. A. ElGawady, “Performance of bridge piers under vehicle collision,” *Engineering Structures,* vol. 140, pp. 337–352, 2017, doi: 10.1016/j.engstruct.2017.02.054.

[30] T. V. Do, T. M. Pham, and H. Hao, “Dynamic responses and failure modes of bridge columns under vehicle collision,” *Engineering Structures*, vol. 156, no. November 2017, pp. 243–259, 2018, doi: 10.1016/j.engstruct.2017.11.053.

[31] K. Heng, R. Li, and H. Wu, “Damage Assessment of Simply Supported Double-Pier Bent Bridge under Heavy Truck Collision,” *Journal of Bridge Engineering*, vol. 27, no. 5, pp. 1–22, 2022, doi: 10.1061/(asce)be.1943-5592.0001851.

[32] G. Liu, “Behavior of bridge piers during vehicular impacts,” City College of New York, The City University of New York, 2012.

[33] R. Cao, “Heavy truck collision with bridge piers,” City College of New York, The City University of New York, 2019.

[34] C. E. Buth, W. F. Williams, M. S. Brackin, D. Lord, S. R. Geedipally, and A. Y. Abu-Odeh, “Analysis of Large Truck Collisions with Bridge Piers: Phase 1, Report of Guidelines For Designing Bridge Piers and Abutments for Vehicle Collisions,” Texas Transportation Institute, 2010.

[35] Y. Zhou et al., “Pendulum impact loading tests of precast concrete columns with various column base connections,” *Engineering Structures*, vol. 252, Feb. 2022, doi: 10.1016/j.engstruct.2021.113736.

[36] W. Sun, C. Yang, W. Fan, H. Wang, and H. Su, “Vehicular impacts on precast concrete bridge piers with grouted sleeve connections,” *Engineering Structures*, vol. 267, Sep. 2022, doi: 10.1016/j.engstruct.2022.114600.

[37] H. Su, W. Fan, H. Wang, B. Liu, W. Sun, and X. Shao, “Direct shear strength of UHPC-based gravity-type grouted sleeve connection members,” *Journal of Building Engineering*, vol. 69, Jun. 2023, doi: 10.1016/j.jobe.2023.106266.

[38] G. C. Lee, Z. Liang, J. J. Shen, and J. S. O’Connor, “Extreme load combinations: A survey of state bridge engineers,” MCEER, University at Buffalo, State University of New York., 2011.

[39] Z. Lu et al., “Mechanical behaviour of grouted sleeve splice under uniaxial tensile loading,” *Engineering Structures*, vol. 186, pp. 421–435, May 2019, doi: 10.1016/j.engstruct.2019.02.033.

[40] C. P. Pantelides, M. J. Ameli, and L. D. Reaveley, “Evaluation of Grouted Splice Sleeve Connections for Precast Reinforced Concrete Bridge Piers (MPC-17-320),” 2017.

[41] E. Henin and G. Morcous, “Non-proprietary bar splice sleeve for precast concrete construction,” *Engineering Structures*, vol. 83, pp. 154–162, Jan. 2015, doi: 10.1016/j.engstruct.2014.10.045.

[42] Y. Li, L. Zhang, Q. Zhang, X. He, J. Wang, and Y. Su, “Anchorage behavior of grouting sleeves under uniaxial and cyclic loading–A comparative study of the internal structure of sleeves,” *Journal of Building Engineering*, vol. 49, May 2022, doi: 10.1016/j.jobe.2022.104057.

[43] G. Zheng, Z. Kuang, J. Xiao, and Z. Pan, "Mechanical performance for defective and repaired grouted sleeve connections under uniaxial and cyclic loadings," *Construction and Building Materials*, vol. 233, Feb. 2020, doi: 10.1016/j.conbuildmat.2019.117233.

[44] T. Guo, J. Yang, W. Wang, and C. Li, "Experimental investigation on connection performance of fully-grouted sleeve connectors with various grouting defects," *Construction and Building Materials*, vol. 327, Apr. 2022, doi: 10.1016/j.conbuildmat.2022.126981.

[45] Z. Zhang, S. Jiang, W. Cai, and C. Zhang, "Effects of Grout Compactness on the Tensile Behavior of Grouted Splice Sleeve Connectors," *Applied Sciences (Switzerland)*, vol. 12, no. 9, May 2022, doi: 10.3390/app12094595.

[46] Z. B. Haber, "Precast Column-Footing Connections for Accelerated Bridge Construction in Seismic Zones," University of Nevada, Reno, 2013.

[47] C. Liu, L. Pan, H. Liu, H. Tong, Y. Yang, and W. Chen, "Experimental and numerical investigation on mechanical properties of grouted-sleeve splices," *Construction and Building Materials*, vol. 260, Nov. 2020, doi: 10.1016/j.conbuildmat.2020.120441.

[48] M. J. Ameli and C. P. Pantelides, "Seismic Analysis of Precast Concrete Bridge Columns Connected with Grouted Splice Sleeve Connectors," *Journal of Structural Engineering*, vol. 143, no. 2, Feb. 2017, doi: 10.1061/(asce)st.1943-541x.0001678.

[49] R. D. Barton, M. J. Ameli, and C. P. Pantelides, "Precast Concrete Bridge Column-Footing Connections with Recessed Grouted Splice Sleeve Connectors," *ACI Structural Journal*, vol. 119, no. 1, pp. 215–226, 2022, doi: 10.14359/51734218.

[50] Z. Liu, H. Lei, T. Tong, S. Wu, and G. Lu, "Precast segmental piers: testing, modeling and seismic assessment of an emulative connection based on a grouted central tenon," *Bulletin of Earthquake Engineering*, vol. 20, no. 5, pp. 2529–2564, Mar. 2022, doi: 10.1007/s10518-022-01335-w.

[51] Mostafa Tazarv, "Next Generation of Bridge Columns for Accelerated Bridge Construction in High Seismic Zones," University of Nevada, Reno, 2014.

[52] ASTM Standard A536-84, *Standard Specification for Ductile Iron Castings*. West Conshohocken, PA, USA: ASTM International, 2014. doi: 10.1520/A0536-84R19E01.2.

[53] ASTM Standard C39, *Standard Test Method for Compressive Strength of Cylindrical Concrete Specimens*. West Conshohocken, PA: ASTM International, 2012. doi: 10.1520/C0039.

[54] ASTM Standard C109, *Standard Test Method for Compressive Strength of Hydraulic Cement Mortars (Using 2 in. or [50-mm] Cube Specimens)*. West Conshohocken, PA: ASTM International, 2012. doi: 10.1520/C0109.

[55] ACI-318-08, *Building Code Requirements for Structural Concrete, in American Concrete Institute*. American Concrete Institute: Farmington Hills MI, 2008.